Politecnico di Torino

Corso di Laurea Magistrale in Ingegneria Biomedica

When CT images come without calibration phantom: phantom-less calibration procedure for FE-based prediction of fracture risk

Supervisors:

Dr. Mara Terzini

Dr. Alessandra Aldieri

Author:

Antonio Carmine Moretta

Anno accademico 2020/2021

Index

ABSTRACT

Osteoporosis affects a huge number of people and its prevalence is expected to increase. The gold standard for its diagnosis, the Bone Mineral Density (BMD)-based T-score, has not proven accurate enough for its prediction: the need to find new methods able to improve fracture risk estimation is therefore urgent. In this context, aiming to improve hip fracture risk detection, Computed Tomography (CT)-based Finite Element (FE) models have been shown to predict femoral fracture risk more accurately thanT-score. In the development of CT-based FE analyses, the calibration of the CT images, fundamental to extract local BMD values related to the Hounsfield Units (HU) values, is commonly based on the availability of a calibration phantom: however, it is not always possible to have phantoms available in the clinical practice. When that happens, phantom-less calibration represents the only viable option. The aim of this thesis was to implement an alternative phantom-less calibration of CT images to extract local BMD values from HU in absence of a calibration phantom. CT images of the proximal femurs for a cohort of 28 post-menopausal women were examined, aiming to build CT-based 3D patient-specific models for hip fracture risk estimation. Since the CT images came without the calibration phantom, a phantom-less calibration procedure selected from the literature was followed to calibrate them so that local material properties could be assigned to the FE models. Peaks of air, fat and muscle tissue were extracted from histograms of the HU in a region of interest for each patient. These peaks were linearly fitted to reference BMD values of the corresponding tissues in order to extract a patient-specific calibration of the images. Thus, HU-BMD calibration functions could be identified; subsequently, these calibration functions were employed to assign material properties to the FE models. Boundary conditions reproducing sideways fall conditions were eventually applied and static simulations performed. Tensile and compressive principal strains were extracted for the models and a Risk Factor (RF) calculated for each mesh element as the ratio between principal strains and corresponding thresholds. Furthermore, a

Risk Factor Index, (RFI), the highest superficial RF value, and the Femoral Strength (FS), the load at which fracture was estimated to occur, were extracted for each patient. The obtained outcomes were comparedwith those obtained from analogous models where the equivalent local densities were obtained with a literature-based non-patient-specific calibration. The corresponding element-specific principal strains and RF values were compared and relative errors computed. As far as principal strains and RF are concerned, the mean relative error considering the patient-specific average errors values were between 25 and 26%, while the maximum value among the average ones for each patient were between 31% and 34%. The fracture risk indicators (RFI and FS) turned out to be significantly correlated ($p<0.05$), but a greater number of patients resulted to be at high fracture risk according to the phantom-less and patient-specifically calibrated models. Unfortunately, the lack of follow-up information did not allow the validation of the obtained results, but in the future further studies will allow the evaluation of the power of the proposed methodology.

CHAPTER 1

INTRODUCTION

1.1 Pathophysiology of Osteoporosis

Osteoporosis, that means “porous bone”, has been defined as a skeletal disorder characterized by compromised bone strength, predisposing a person to an increased risk for fracture. It is the most common bone disease in humans, representing a major public health problem [1].

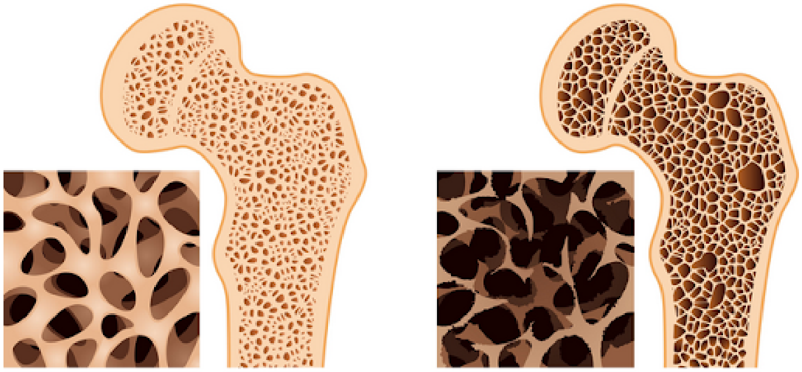

Figure 1.1: healthy bone (on left) vs osteoporosis bone (right)

Bone is a dynamic tissue that is continuously removed and replaced in order to ensure adaptation of the skeleton to weight-bearing, repair micro-damages that result from mechanical stresses and allow for mobilization of calcium from the skeleton in order to maintain serum calcium homeostasis. Bone remodeling is initiated by the development and activation of osteoclasts, the bone-resorbing cell, which then release growth factors capable to activate osteoblasts, the bone-forming cell.

The activities of bone removal and deposition are coupled within each bone multicellular unit [2]. Some factors, as menopause and advancing age cause an imbalance between resorption and formation rates, where the resorption becomes higher than absorption, thereby increasing the risk of fracture due to bone loss.

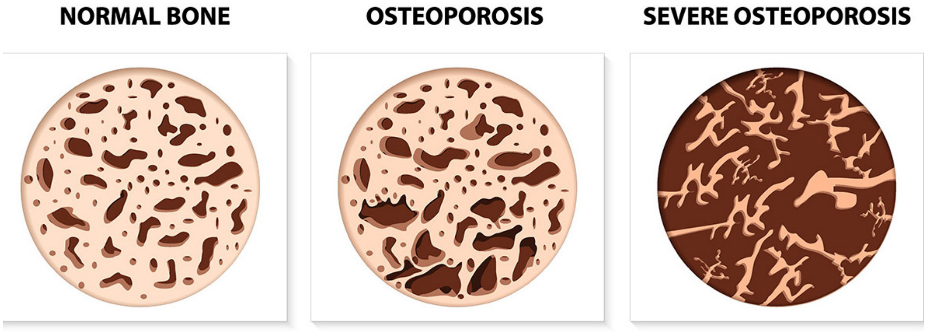

Figure 1.2: stages of osteoporosis

Osteoporosis can be classified into two main groups by considering the factors affecting bone metabolism:

- Primary osteoporosis, that is further classified into Type I, associated to menopause and oestrogen deficiency, and Type II osteoporosis, which affects both men and women older than 70 years[3].
- Secondary osteoporosis, that might ensue a number of disorders, such as endocrine, hematopoietic or renal diseases, and medications.

Due to the cohort included in this thesis, made up of post-menopausal women, primary osteoporosis will be the main focus of the work.

This pathology affects an enormous number of people, of both sexes and all races, and its prevalence will increase as the population ages. It is a silent disease until fractures occur, which causes important secondary health problems and even death. It was estimated that the number of patients worldwide with osteoporotic hip fractures is more than 200 million [1]. Fractures and their complications are the relevant clinical sequelae of osteoporosis. A recent fracture at any major skeletal site, such as vertebrae (spine), proximal femur (hip), distal forearm (wrist), or shoulder in an adult older than 50 years with or without trauma, should suggest that the diagnosis of osteoporosis needs further urgent assessment involving diagnosis and treatment. Fractures may cause chronic pain, disability and death.

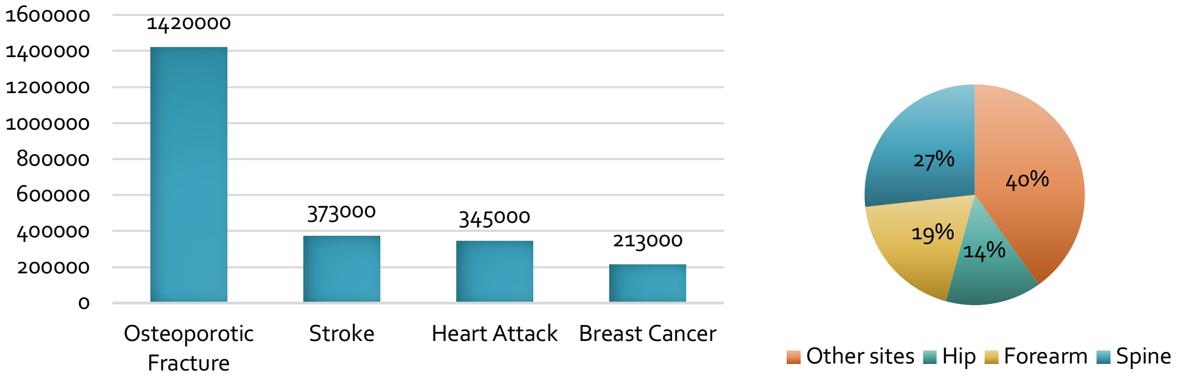

Figure 1.3: On left: Annual comparative incidences of osteoporosis-related fractures, new strokes, heart attacks, and invasive breast cancer in women in the United States between 2004 and 2006[1]. On right: Subdivision of osteoporotic fractures

Hip fractures are cracks or breaks in the top of the thigh bone (femur) close to the hip joint. They are usually caused by a fall or an injury to the side of the hip, but may occasionally be caused by a health condition. In 1990, the number of hip fracture worldwide was estimated to be 1.66 million [4], comprising around 1.19 million in women and 463000 in men. In the UK around 79000 individuals suffer hip fractures each year, with a cost in 2010 estimated at £3.5 billion projected to rise £5.5 billion per year by 2025 [4].

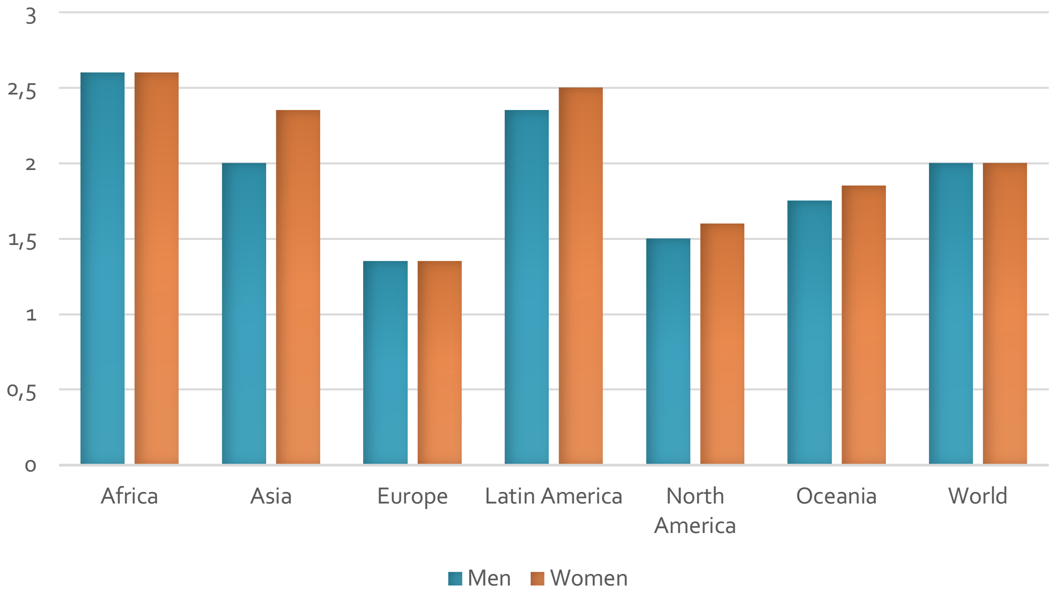

Figure 1.5: Number of men and women at high fracture risk in 2040 relative to 2010, by world region [4]

An osteoporotic fracture describes a fracture event arising from trauma that in a healthy individual would not give rise to fracture. The most common fractures defined in this way are those at the hip, spine, and forearm, but many other fractures after the age of 50 years are related at least in part to low BMD and should be regarded as osteoporotic. These include fractures of the homer, ribs, tibia, pelvis and other femoral fractures. Hip fractures is the most serious osteoporotic fracture, in fact the mortality burden of hip fracture is significant, with a rate of approximately 8% in men and 3% in women aged above 50 years and hospitalized following fracture. In the USA, approximately 31000 annual deaths occur within 6 months of hip fracture[4]. According to the National Health and Nutrition Examination Survey III, conducted from 2005 to 2010, over 10.2 million adults had osteoporosis and more than 43.4 million adults had low bone mass in the USA.

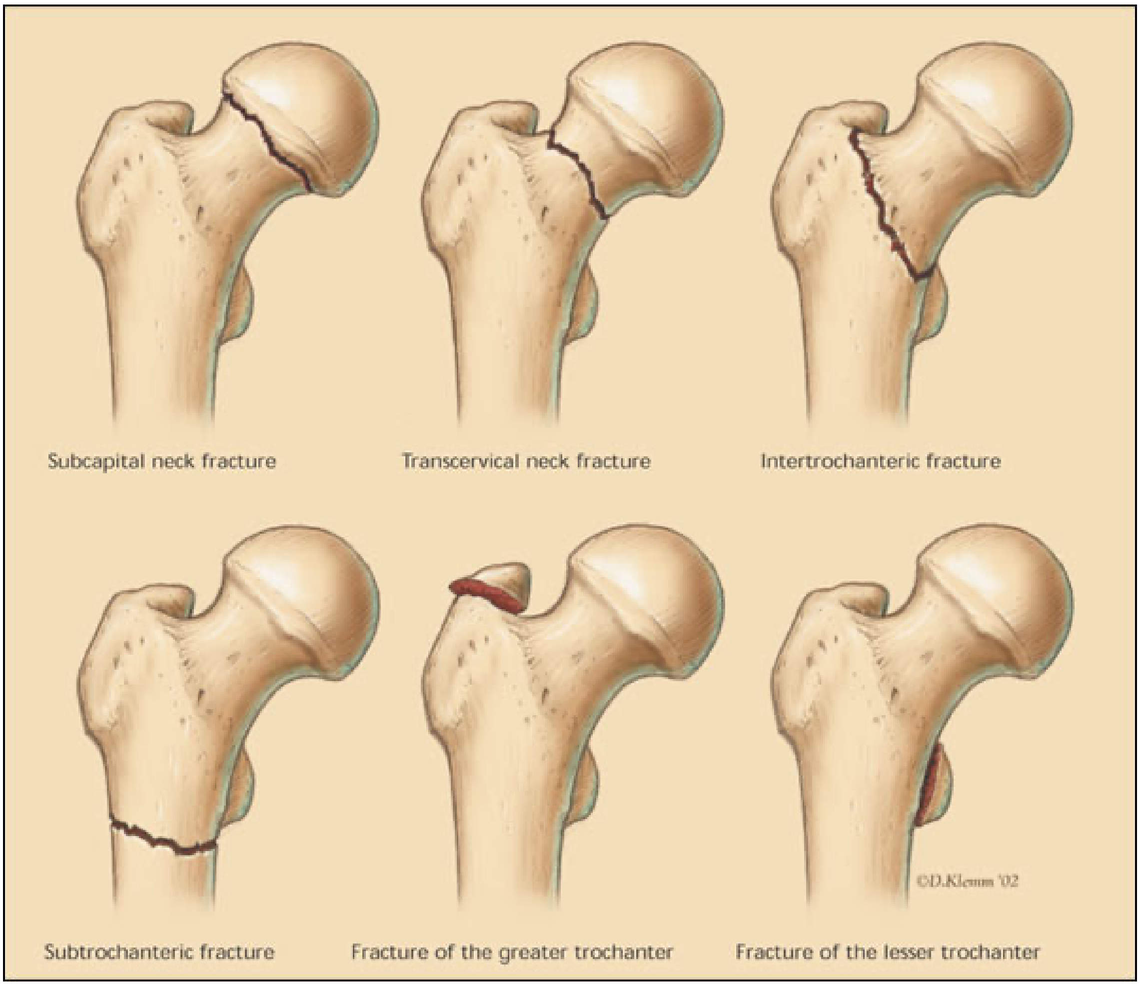

Figure 1.4: example of hip fractures

With the aging of the population, this number will only become larger increasing both the rate of osteoporosis diagnoses and the risk of fracture [2]. The economic burden of osteoporosis-related fracture is significant, costing approximately $17.9 and £4 billion per annum in the USA and UK respectively, when in the Table 1.1 are summarized fracture impact across the European Union [4]. Clinically, hip fractures represent the most serious osteoporotic connected occurrence, because of both related costs and outcomes [5].

	Hip	Spine	Wrist
Lifetime risk in women (%)	23	29	21
Lifetime risk in men (%)	11	14	5
Cases/year	620000	810000	574000
Hospitalization (%)	100	2-10	5
Relative survival	0.83	0.82	1.00
Costs: All sites combined ~ €37 billion			

Table 1.1: impact of osteoporosis-related fractures across Europe

The risk of hip fracture depends on two events:

- the proximal femoral structural strength, that is the minimum force on the femoral head that could to break the proximal femur, also known as hip bone strength or hip fracture load;
- the probability of encountering a situation in which the force applied to the proximal femur exceeds the proximal femoral structural strength [6].

The strength of the proximal femur depends strongly on the three-dimensional (3-D) geometry of the bone and the 3-D distribution of the material properties within the bone as well as the direction and location of the applied force.

1.2 Diagnosis of Osteoporosis

The osteoporosis is analysed with densitometry techniques, in particular the gold standard for osteoporosis screening is dual energy x-ray absorptiometry (DEXA) according to World Health Organization (WHO)[7]. This technique uses x-rays physical principles which yields a 2D-areal bone mineral density (aBMD). However, the representative aBMD cannot be a perfect stand-alone measure of bone strength because it neglects the 3D bone structure. An alternative non-invasive screening process is Quantitative Computed Tomography (QCT) which uses a calibration phantom to evaluate the bone mineral content of a given bone by comparison and yields volume-based BMD (vBMD) results from CT images or a true physical density of mass per volume.

Figure 1.6: example of DEXA (on top) and qCT (on bottom)

In contrast to aBMDs, voxelwise volumetric BMDs can provide a spatial BMD distribution in 3D, thereby eliminating the sources of errors in estimating bone strength. DEXA and QCT fundamental principle is the variable absorption of X-rays by different body components. Measuring the attenuation of X-rays with high- and low-energy photons, the bone can be distinguished from soft tissues and the mineralized bone mass eventually assessed neglecting surrounding soft tissues attenuation effect. The attenuation is expressed in Hounsfield Unit (HU). The measurement of attenuation with DEXA does not allow the determination of the volume in which the mineral bone is distributed. In fact, this projective technique is based on the two-dimensional representation of the bone structure examined. Therefore, different anatomical regions are represented as on a frontal plane with the result of obtaining an integrated measurement that includes the cancellous bone, the compact bone and any other calcified formations of the soft parts, included in the path of the radiant beam, in the poster-anterior projection.

The information derived from bone densitometry techniques are as follows:

- measurement of the thickness of the cortical bone (mm);

- measurement of the volume of the studied area (cm^3);

- measure of bone mass (g);

- measurement of the bone mineral content (Bone Mineral Content-BMC expressed in g / cm);

- measurement of bone mineral density in an area (Bone Mineral Density-BMD expressed in g / cm^2);

- measurement of bone mineral density in a given volume (BMD expressed in mg / cm^3). The measurement of a bone volume (mg / cm^3) is obtained only with qCT.

The World Health Organization established the criteria of a densitometry analysis with reference to the values obtained using a DEXA equipment in lumbar and femoral scans. However, these criteria have also been widely applied to the results from other types of scans allowed by DEXA technology such as total body and ultra-distal radio and by other methods that use X-rays such as QCT.

The criteria proposed by the WHO arose from the analysis of a huge database made up of groups of individuals of different ages, sexes and races. Bone densities, estimated by DEXA, is given to patients as a T-score or a Z-score and the adopted criterion from WHO classifies individuals on the basis of the T-score (Table 2). The T-score represents the standard deviation (SD) of the patient-specific BMD, compared with young standard population of the same sex.

Category	**T-score**
Normal	T-score > 1
Osteopenia	-2.5 <T-score< -1
Osteoporosis	T-score < -2.5
Severe osteoporosis	T-score < -2.5 with fractures

Table 1.2: classification of osteoporosis

The T-score therefore represents the difference between the bone mass of the patient examined and the average bone mass of the reference youth population and is expressed in terms of standard deviation from the youth population. If the examined subject is compared with the bone mass of the reference population of the same age, the Z-score is obtained. This parameter is recommended in the evaluation of subjects over 80 years of age. BMD has been shown to be a strongest risk factor for fractures and for this reason the T-score is considered for the diagnosis of osteoporosis. Therefore, osteoporotic clinical diagnosis is based on BMD, but the important clinical significance of the pathology is to know what causes the fracture and treatments have to the decrease the risk of it. Because the majority of the patients suffering from low-trauma fractures are not classified as osteoporotic according to T-score [3], there are other thresholds for pharmacological intervention. Some of other clinical risk factors that are able to support the risk of fracture prediction are: age, low BMI, the presence of prior fractures, smoking, use of glucocorticoids and alcohol intake [4]. Important risk factors, associated to clinical risk, are geometry and distribution of bone mass that influence the bone strength. Moreover, there are recently new tools that are obtained by DEXA and are based on T-score, such as Hip Structural Analysis (HSA) and Trabecular Bone Score (TBS). TBS gives more information about the trabecular microarchitecture quality analysing the pixel intensity variations, while HSA is a technique that uses the properties of dual energy x-ray absorptiometry images to derive geometric parameters for the hip that are associated with bone strength [8]. Bone strength depends on two parameters: bone quality (bone architecture) and bone quantity (bone mineral density).

1.3 Finite Element Analysis of CT images

In addition to DEXA, other methods have been proposed that identify individuals at high risk of fracture including those that characterize volumetric bone density, in particular recent studies uses the finite element analysis of CT images [9]–[12]. CT images finite element analysis (CT - FEA), that incorporates information about architecture and bone density distribution, provides non-invasive estimates of bone strength and Finite element (FE) models have shown to be promising as a tool for fracture risk prediction [13]. In particular, the combination of FE and CT appears promising to identify patients at high risk of fracture [5]. Computed Tomography (CT) scans can be used to segment patient-specific bone geometries that serve as input for the FE models. Basically, this numerical technique subdivides a structure into many smaller parts (finite elements) that represent the complex material heterogeneity and 3-D bone geometry as a mathematical model. Force or displacement is then mathematically applied to represent a specific loading condition. When the model is analysed, stress and strain throughout the structure are computed and used in conjunction with material failure criteria to estimate the strength of the proximal femur under the particular loading condition.

Some retrospective studies have demonstrated that FE-based femoral strength is predicted as measured ex vivo with excellent accuracy [13]–[16] and is a better predictor of fracture risk than the aBMD [9]. Actually, there are different modelling approaches about the FE studies of proximal femur fracture. The FE models are obtained from CT images, where the bone is segmented from the CT scan data and converted into voxel-based FE models. The segmentation of images can be manual, semi-automatics [17] or can be done developing automatic algorithms [18], [19]. After the segmentation the models are meshed and then material properties are assigned to the mesh elements by converting vBMD or equivalent CT density using empirically derived relationships. To map material properties from CT images into FE models the first step is to employ the calibration to obtain local bone mineral density from HU values (that will be explained in the next subchapter). With the HU-local bone mineral density calibration the material properties are assigned to mesh elements using density-elasticity relationships specified for the considered anatomical district to estimate Young modulus. The relationship between densities and elastic modulus for cortical and trabecular bone are given by experimental and validated methods[20]. There are different approaches of density-mechanical property relationship in literature that are related to physical methods adopted: some studies are based on ash density[21]–[24], other studies employed apparent density [25][26], others utilize a combination of this both densities [27]–[29] and recent studies are utilizing tissue density [20]. Subsequently at the material assignment, boundary conditions are applied to the models miming some loading conditions to predict the strengths and the failure loads of FE model. Different loading conditions are evaluated in previous studies about hip fractures: axial loads that mimics the hip joint reaction in physiological stances [13], [14], [30], [31], forces that simulate sideways fall [32]–[34] or both configurations [35]. To estimate bone stiffness reaction forces and displacement data are used, while the failure load is estimated from the selected failure criteria. Having an optimal accuracy about strain prediction is fundamental to analyse bone properties and eventually to estimate fracture risk fractures. About accuracy is important to use appropriate mathematical laws for the anatomical region treated and to follow the protocol scanner settings [20]. Most importantly, the various effects of scanning protocol have been further investigated and the correlation between the HU and BMD values is dependent on X-ray tube peak voltage (kVp) of the scans, on the CT scanning region and if are present also on the contrast medium [36]. So, is fundamental to follow the same scanner settings to have good model accuracy.

1.4 Phantom and phantom-less calibration using CT scans

CT is a non-invasive technique that uses the attenuation of x-rays with matter in order to obtain detailed images on internal organs. This phenomenon follows Lambert-Beer's exponential law: $I = I_0 e^{-\mu x}$, where x is the thickness of the object investigated and μ is the attenuation coefficient. Each pixel in the detected image is assigned a numerical value (CT number) corresponding to the average attenuation coefficient of the corresponding voxel. These CT numbers are shown on an arbitrary unit scale, that is called Hounsfield unit, with a linear transformation according to the formula:

$$CT\ Number\ (HU) = 1000 * \frac{\mu_x - \mu_{water}}{\mu_{water} - \mu_{air}}$$

where μ_{water} and μ_{air} are relatively the attenuation coefficient of water and air.

The diagnostic capability of CT scan in metabolic bone disease depends on the accuracy of measurement of the bone mineral contained within the organ body investigated. Accuracy is influenced by the attenuation coefficients and the model assumed for bone composition. Proper calibration of the scan is required to correct for variations in scanner settings and attenuation, any related beam-hardening, and patient-specific characteristics such as body size, all of which can alter the attenuation characteristics [37]. Most scanners incorporate some filters to correct these artefacts due to improve image quality [38]. The measurement of voxelwise BMD is critical to conduct a reliable finite element analysis because the elastic moduli of each finite element need to be derived through the BMD-modulus relationship.

Hounsfield units (HU) in the CT scan can be converted to bone mineral densities (BMD) that are used to model element-specific bone material properties. The most widely used method for calibrating CT scans, converting HU to BMD, utilizes an external calibration phantom. Currently, these conversions to BMD are usually done with either solid or liquid phantom that contain certain known concentrations of for example calcium hydroxyapatite ($CaCO_3$ or CaHA) or hydrogen dipotassium phosphate (K_2HPO_4 or KHP). The type of phantom provides the density-elasticity law due to the different physical properties, it is fundamental for the accuracy of FEM development.

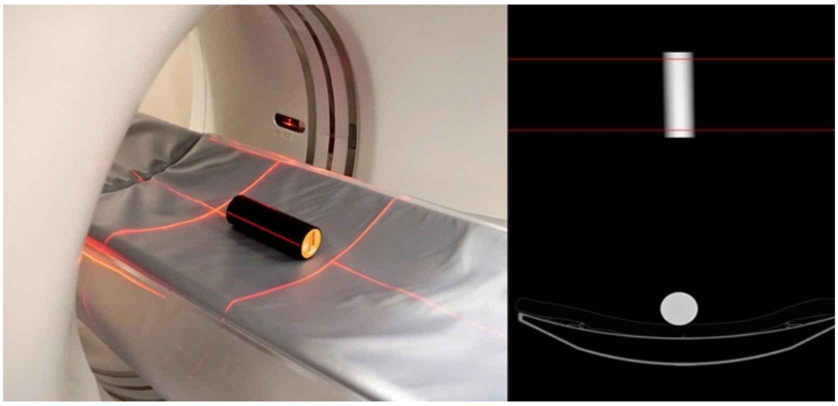

Figure 1.7: phantom calibration

Usually, the patient is scanned with face upward and lying on a phantom. The need for a phantom adds expense and increases the logistical burden of clinical imaging. To improve the phantom technique have been developed methods without a calibration phantom for calibrating CT scans, specifically three approaches are mostly followed: some studies uses calibration factors [39], where firstly the calibration functions are obtained from a separate scan of a calibration phantom offline, the factor (called GCF) is obtained with the ratio of the BMD derived from the calibration offline divided by the respective HU numbers. The phantom-less BMD values are calculated multiplying the GCF with HU values; another phantom-less option is to use patient-specific internal calibration methods, which are based on HU of specific tissues, such as fat and muscle tissue or external air and either aortic blood or visceral fat; finally, another approach is to use CT numbers (HU) directly [40][41] where there are specific software that automatically detect the relevant FE models factors. Studies comparing phantom calibration with phantom-less calibrations showed that they yielded comparable results [42], however phantom-less approaches show some limitations. The first approach is CT scanner and protocol specific, but for other scans is not specific and is not precise enough for finite element analyses. The limitation of the second approach is the poor repeatability, presumably due to the challenges of choosing the region of muscle in a repeatable fashion as well as consistently separating out the pure tissue components [43]. In addition, the assumption of specific densities for internal tissues could influence the measurement of CT numbers, due to the possible presence of pathologies. Finally, the third approach could be the more affordable in clinical practice, but needs significant amounts of patient case studies [44] to be applied in FEA.

1.5 Purpose of the thesis

Osteoporosis is an increase disease in our society, as evidenced by the rising numbers of cases and the economic outlay for treatments. Hip fractures are among the most serious complications of osteoporosis, with devasting aftermaths the quality of life, morbidity and mortality, as well as economically on healthcare systems. The accuracy of the prognostic standard of bone densitometry, based on T-score, is too low to diagnostic the pathology and to adopt therapeutic treatments. In this context, aiming to improve hip fracture detection, CT-based FE models, able to combine patient-specific geometry and material properties, have been shown to achieve optimal accuracy on the prediction of femoral fracture risk more accurately than the actual gold standard. Phantom-based calibration is the gold standard in the development of CT-FEA in order to calibrate CT images (HU) for extracting local BMD values, but is not always possible to have phantoms available together with the CT images in clinical practice. The goal of the present study is to propose an alternative strategy to calibrate images in absence of calibration phantoms. Specifically, the target is to determine a correlation between the HU obtained from computed tomography scans and local bone mineral density, implementing a phantom-less calibration and developing a structural model technique that predicts proximal femoral strength with a finite element analyses. The choice to apply the phantom-less calibration depends on the impossibility of using a calibration phantom and phantom-less tool represent the only viable option when the phantoms are not available. Therefore, it was not possible to follow the standard procedure and the phantom-less CT scan calibration was derived following previous studies in the literature. In this thesis, CT images of the proximal femurs for a cohort of 28 post-menopausal woman were assessed, with the aim to build CT-based three dimensional patient-specific models for hip fracture risk estimation. In order to calibrate them, to assign local material properties to the FE models, calibration equations are obtained applying a pseudo-calibration. Then these are employed to patient scans to calculate local BMD from HU values. In particular, the performance of this method are compared with analogous models obtained with a different method to calibrate CT images and BMD that is not patient-specific. The relation between HU and BMD gives the material properties that are the input for FE analyses. These analyses are done in order to further asses the correlation between material density, the HU value and mechanical strength. In detail, boundary conditions reproducing a sideways fall were performed on patient-specific models of the proximal femur and static simulations were executed. The purpose of the simulations with a post-processing phase is to predict surface strains on the proximal femur and to obtain indicators that could estimate hip fractures. The effects of calibration on the estimation of fractures are evaluated comparing the principal strains and fracture loads obtained from FE models. This study stems from the growing need to try new tools that could be useful in clinical practice as support to the T-score based-criteria. Although it was not possible to validate the obtained results, because the analysis could not be done retrospectively, the methodologies applied on our cohort show important differences about the influence of calibration and the ambition is to extend them at a cohorts with follow-up information.

CHAPTER 2

MATERIAL AND METHODS

2.1 CT scans

In the present thesis twenty-eight post-menopausal female subjects have been taken and studied (after they had signed an informed consent). This patients, between 55 and 81 years of age, were treated in San Luigi Gonzaga Hospital in Orbassano, in province of Turin, Italy. From the Hospital database only patients with available clinical data and CT scans were chosen. The CT scanner is *Brilliance 64*, manufactured by Philips and the scans available have not been prescribed for osteoporosis diagnosis purposes. For this reason, only the proximal portion of the femur is included in the images and only people with femur clearly visible in the CT scans are included in this study. Moreover, between the patients have been excluded patients suffering by cancer, due to the possible presence of bone metastasis, which would affected bone strength, probably due to unrealistically strong material properties in the FE model because of the high degree of mineralization in blastic lesions [42]. CT images of patients were obtained with this settings: 120 kVp, 220 or variable mA, the slices thickness was 2 mm and the pixel width was 0.6857 mm.

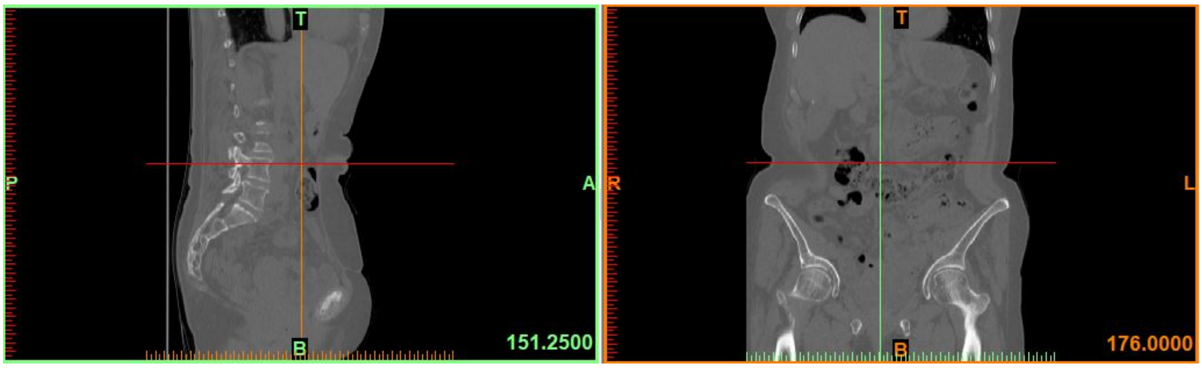

Figure 2.1: example of CT images from *Mimics Medical 19.0*

2.2 FE model construction: segmentation, FE mesh and boundary condition

Using the software *Mimics Medical 19.0* it was possible to build the three-dimensional subject-specific geometric models of the proximal femur, with a semi-automatic segmentation. One femur in each patient was segmented to extract the three-dimensional bone morphology. The proximal femur is aligned, following a reference configuration, in according to its anatomical reference system, defined on neck and shaft axes. The 3D models were cut 2.5 cm below the midpoint of the lesser trochanter.

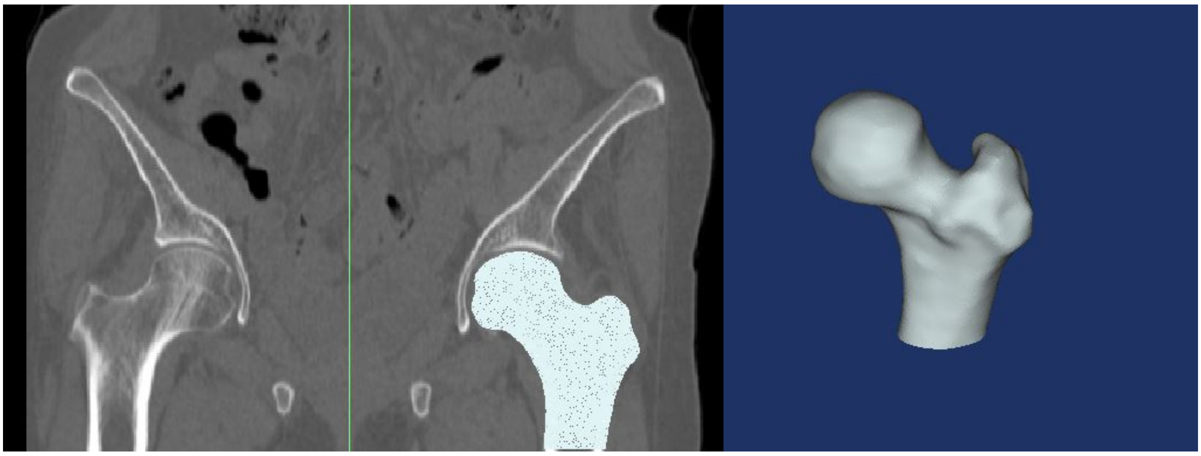

Figure 2.2: an example of FE mesh (left) and an example of FE model femur from *Mimics Medical 19.0*

The models have been meshed with ten-nodes tetrahedral elements (*C3D10 Abaqus elements*) with edge dimensions of 1.2 mm. This value was obtained doing a sensitivity analysis on FE mesh elements dimensions in order to obtain sufficiently accurate results [3].

To incorporate material heterogeneity, at each element in the model was assigned a unique elastic modulus that is determined with a density-elasticity relationship [27] (*Equation 1*), which has been shown to yield accurate strain predictions [30], [45], [46]:

$$E = 15010 * \rho_{app}^{2.18}, \qquad if\ \rho_{app} \leq 0.28\ g/cm^3$$

$$E = 6850 * \rho_{app}^{1.49}, \qquad if\ \rho_{app} > 0.28\ g/cm^3$$

where E is the Young's modulus, expressed in MPa, and ρ_{app} is the apparent density, computed from CT-derived HU values, in g/cm^3 . Specifically, the grey values associated with each element of the volumetric mesh are used to assign local density and elastic modulus values. Due to the impossibility to properly calibrate the available CT images, a pseudo-calibration was performed, aiming to estimate the linear relation between HU and apparent density (ρ_{app}) needed to calculate the relative Young's modulus values.

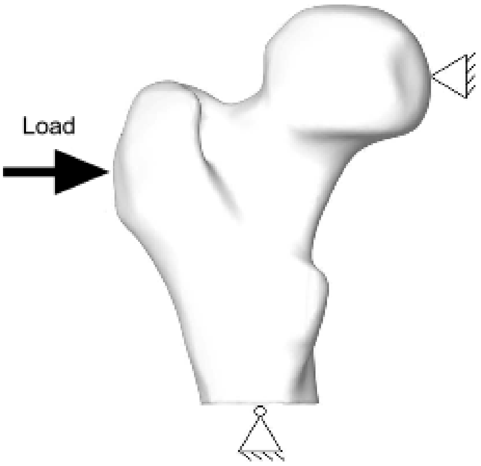

Figure 2.3: boundary conditions applicated to do the mesh dimensions sensitivity analysis [3]

The method adopted in this study for calculating the apparent density followed a previous study present in the literature [43] where calibration of CT images was performed to extract the local BMD values from the images HU both with a phantom and a phantom-less patient-specific procedure. The phantom-less calibration is based on internal patient tissues as calibration reference. To refer to this method we call it *Method PS.* With the available images, which as anticipated before, were obtained for other purposes than this thesis, it was not possible to take the same regions and using the same dimensions to create the volume of interest of the method in the literature [43]. The method mentioned considers a volume with an height of 27 mm, hence we selected a volume with the same height starting from the last slice available in the images, as reported in Figure 2.4.

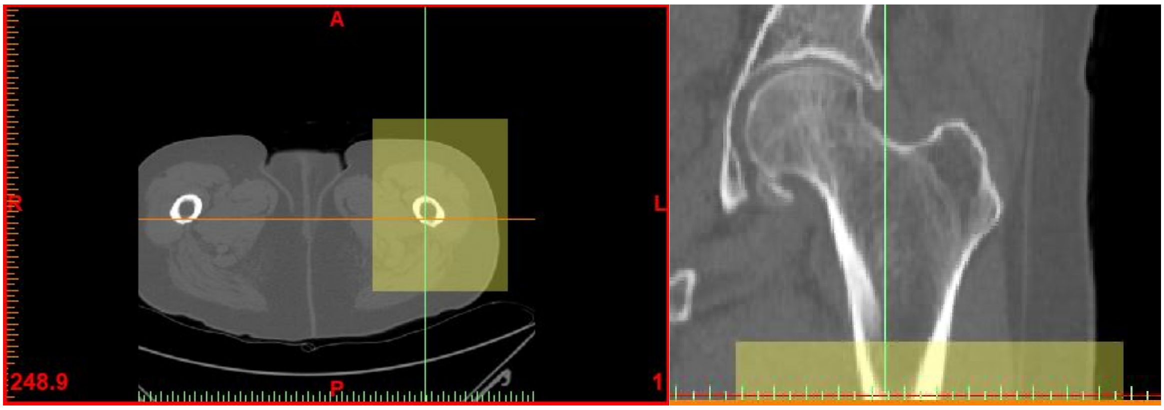

Figure 2.4: example of how is selected the volume of interest from images

To select the volume of interest, as upper limit the lesser trochanter was chosen, but for some patients it was not possible to select a volume with the height settled due to CT images available. The patient with a different volume height are: *patient 4* (8 mm), *patient 10* (10 mm), *patient 21* (14 mm) and *patient 24* (18 mm).

So, for each patient a volume of interest (VOI) was created (Figure 2.4). From the VOI, histograms (Figure 2.5) of the HU values distribution were obtained. To determine the exact peak of HUs for each tissue, the mode of the HU around the histogram peak ($\pm$ 50) HU was calculated, in this way the method was least susceptible to outliers. Due to the impossibility of following and carrying out all the steps, the same BMD values of the method treated in the literature [43] were used: $-840\ mg/cm^3$ for air, $-80\ mg/cm^3$ for fat and $30\ mg/cm^3$ for muscle. These values were obtained with the phantom calibration of the HU peaks of air, fat and muscle of a random subgroup of 10 patient scanned in the study [43] with a Philips scanner, they are also averaged and rounded. The mode of histogram peaks are linearly fitted to the reference BMD values for each patient in order to obtain the air-fat-muscle calibration function.

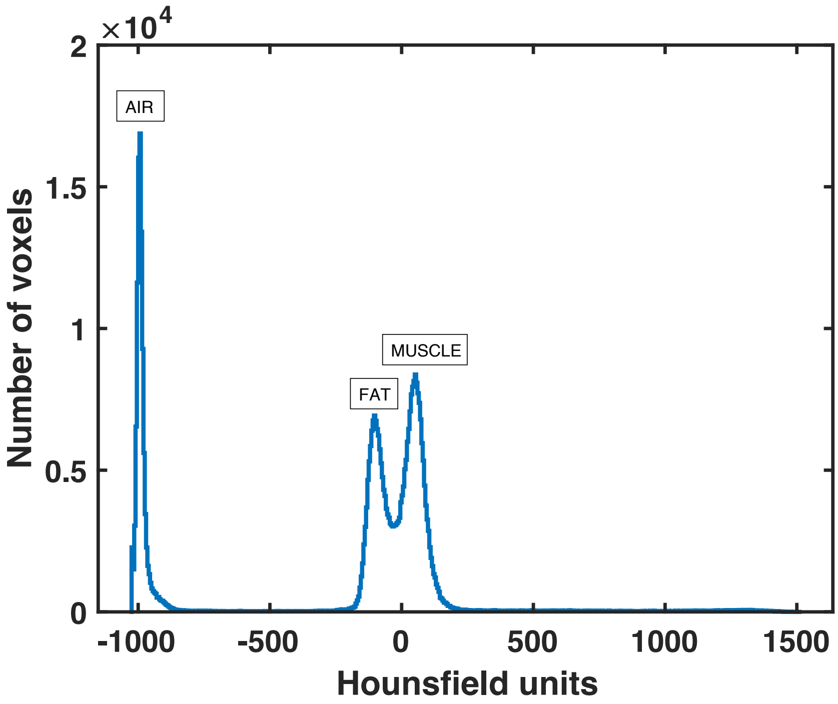

Figure 2.5: example of histogram

Calculating the mode of every peaks ±50 HU and fitting them to the reference BMD values, we obtained a calibration function for each patient (Table 2.1). The equation of calibration is (*Equation 2*): $BMD = a * HU + b \ \ [mg/cm^3]$ (Figure 2.6).

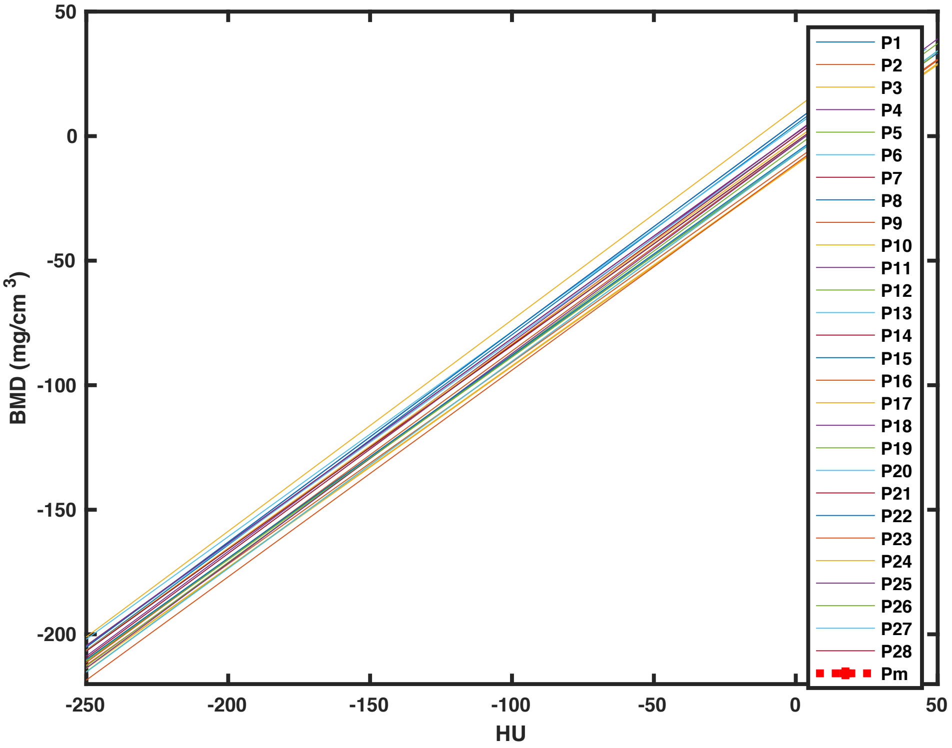

Figure 2.6: all calibration functions for Method PS

Patient	a	b
1	0.844	4.664
2	0.812	-7.271
3	0.808	-11.680
4	0.839	1.214
5	0.813	-7.347
6	0.819	0.054
7	0.838	0.065
8	0.812	-7.199
9	0.810	-9.660
10	0.809	-11.243
11	0.844	5.901
12	0.833	-4.456
13	0.823	3.887
14	0.822	1.034
15	0.844	5.901
16	0.833	-2.856
17	0.820	-1.357
18	0.842	-3.048
19	0.812	-7.247
20	0.817	-2.528
21	0.817	-2.324
22	0.814	-6.572
23	0.829	-10.995
24	0.848	11.102
25	0.822	1.034
26	0.830	-7.358
27	0.831	-7.273
28	0.815	-5.440

Table 2.1: coefficient of calibration function for each patient – Method PS

The calibrated density (converted in g/cm^3) of each voxel in the elements was used to compute the ash density (ρ_{ash}, g/cm^3) from this linear relationship [47]:

$$\rho_{ash} = 0.8772 * BMD + 0.0789 \ (Equation\ 3)$$

and ash density was then used to obtain the apparent density [20] ($\rho_{app}, g/cm^3$):

$$\rho_{app} = 1.58 * \rho_{ash} + 0.00011 \ (Equation\ 4)$$

The apparent densities are used, as reported previously, in the equations of the elastic-modulus to compute mechanical properties for each voxel [27]. The relationships reported are specific to the our anatomic site evaluated, that is the femur.

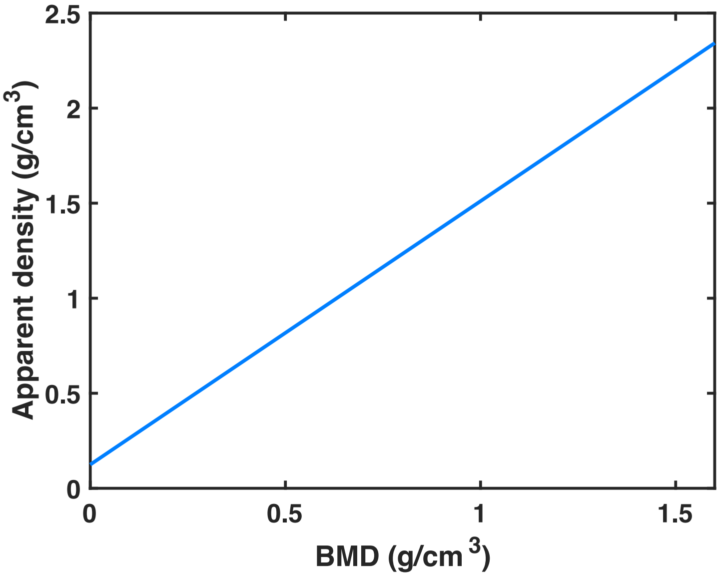

Figure 2.10: example of relation BMD-ρ_{app} considering the vector of central HU (Patient 28) - Method PS

In this study, as anticipated in the previous chapter, two different methods are analysed, specifically two different ways of calculating the apparent density.

Specifically, the *Method PS* is compared with a method that is not patient-specific and that follows a different previous study [3]. To refer to this method we call it *Method nPS.*

In *Method nPS,* a relationship treated in *Ruess et al. (2012)* [21] to applicate a linear conversion between HU values and an equivalent mineral density is used:

$$\rho_{eqm} = 10^{-3}(0.793) * HU\ [g/cm^3]\ (Equation\ 5)$$

From all patients CT images were selected:

- the average highest HU value found in the cortical bone, that is 1200 HU;
- the average lowest HU value of trabecular bone found, that is -140 HU.

These HU values were converted firstly in the equivalent mineral density using *Equation 5*.

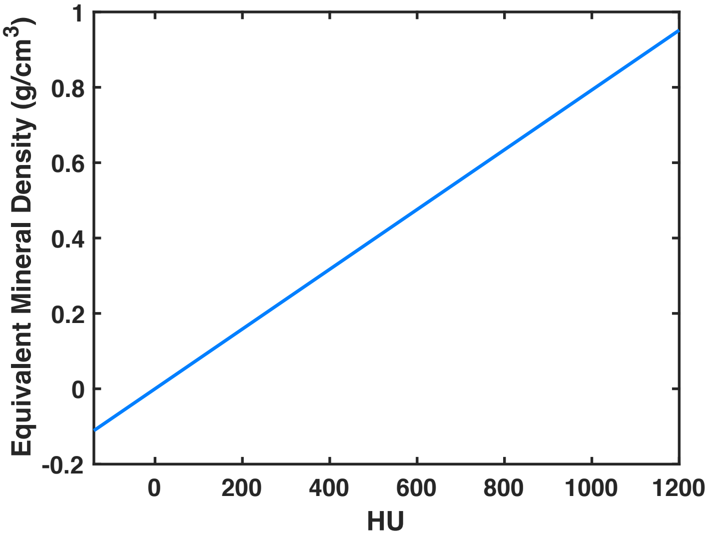

Figure 2.7: relationship $\rho_{eqm} - \text{HU in } \textit{Method nPS}$

Then, the equivalent mineral density was converted in ash density [21]:

$$\rho_{ash} = 1.22 * \rho_{eqm} + 0.0523 \;\; [g/cm^3] \;\; (\textit{Equation 6})$$

Using *Equation 3* apparent density (g/cm^3) was obtained. The average highest HU value found in the cortical bone (1200 HU) and the average lowest HU value of trabecular bone (-140 HU) were fitted with the corresponding apparent densities values (rounded), obtaining the following calibration function:

$$\rho_{app} = 0.0015 * (HU) + 0.2090[g/cm^3] \;\; (\textit{Equation 7})$$

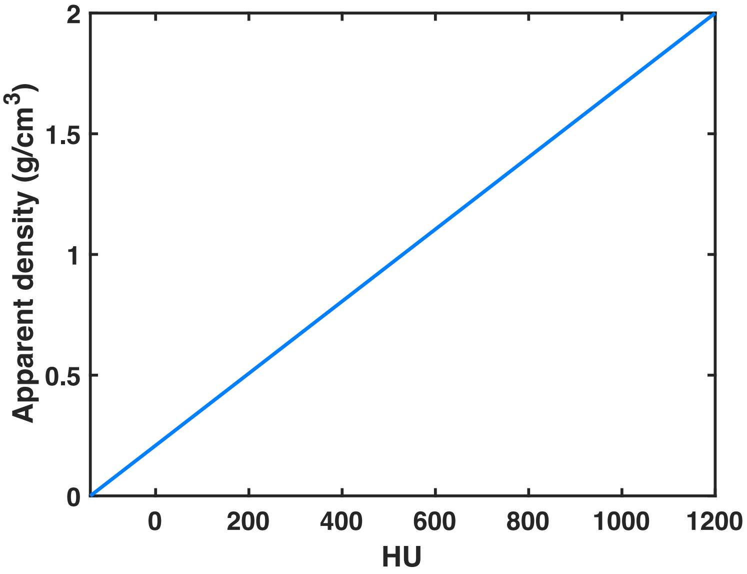

Figure 2.8: calibration function for Method nPS

In this way, patients have the same calibration function. The *Equation 7* is used to obtain the relationship between elastic modulus (MPa) and apparent density (*Equation 1*).

With apparent density-elastic moduli relationship the next step is to allocate the HU-based inhomogeneous material properties at the elements of femur models. To achieve this, the elements of each model were divided into discrete bin based on their associated HU values. To choose the number of HU groups for the assignment of heterogeneous material properties in order obtain accurate results an additional sensitivity analysis was conducted. The analysis was carried out in this way: the highest tensile and the lowest compressive principal strains were computed with different ranges of HU, each ranges contain a different number of discrete bins, specifically, the percentage errors of each range outcomes were computed with respect to the output obtained with the largest number of bins, as reported in Figure 13 [3]. It was chosen a range with 40 different intervals, which is a good compromise for computation and error (< 5%).

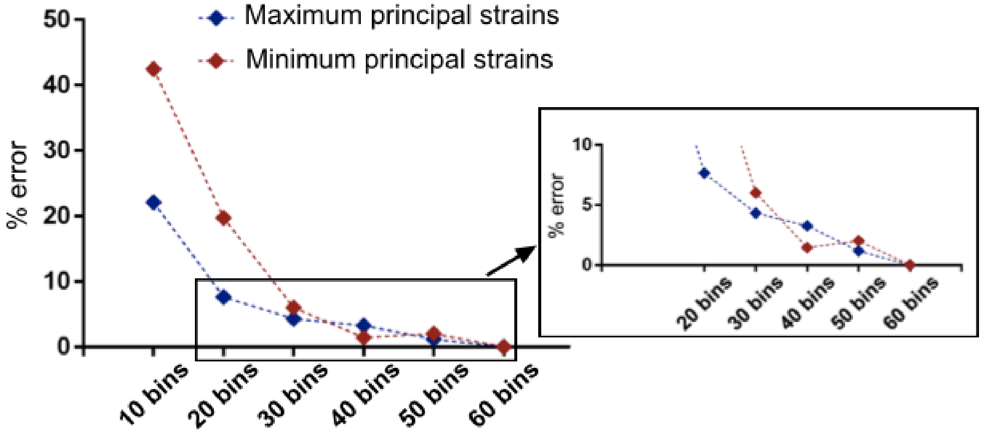

Figure 2.9: sensitivity analysis for the number of HU bins [3]

After the analysis for the dimensions of the mesh elements were assigned the heterogeneous HU-based material properties. To group the HU values in 40 intervals, were calculated the minimum and maximum values of all the HUs patients femoral models considered. From the minimum value to maximum value were obtained 41 extremes (of the intervals), from each interval was calculated an average HU value. In this way there is a vector that contains 40 central HU values where each HU interval represented a material group.

So, an average HU value for each mesh element was first identified and then the total elements HU span was divided into a discrete number of intervals, in order to assign each element to a specific interval on the basis of its own HU value. For each interval, the central HU values through were converted in the correspondent apparent density values with the various mathematical relationship reported and Young's modulus (E) were assigned at each patient femur model. In this way, heterogeneous material properties were mapped into FE models . In order to simulate a fall on the side, following previous studies [30], [32], [34], [48]–[51], the following boundary conditions were applied: load was applied on the greater trochanter, head nodes were restrained along the impact load direction and the distal nodes connected to a hinge. The proximal femur has a linear-elastic behaviour up to fracture, for physiological strain-rates, so was assumed an elastic bone mechanical response [52].

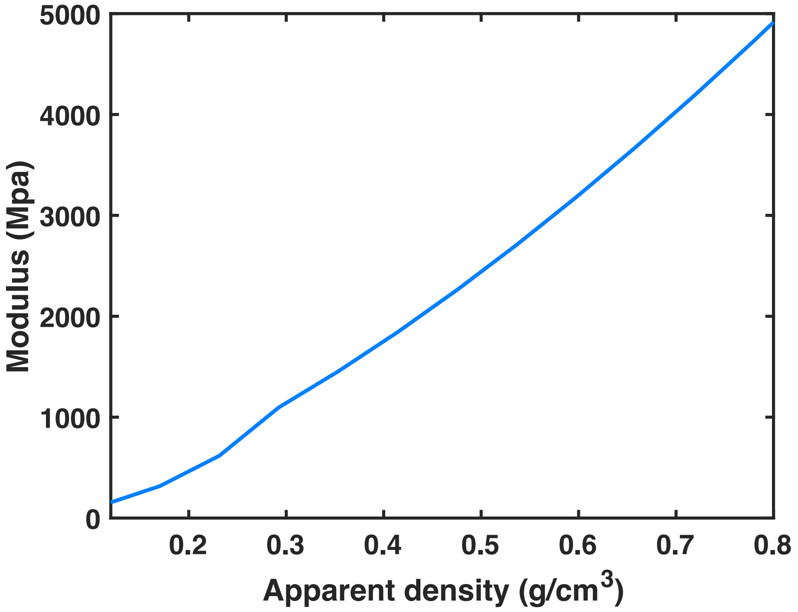

Figure 2.11: example of relation E-ρ_{app} considering the vector of central HU (Patient 28) - Method PS

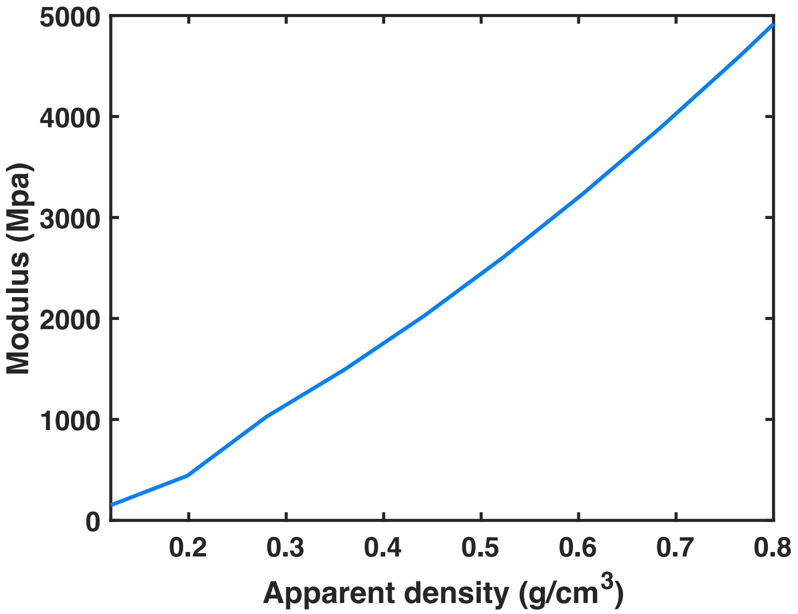

Figure 2.12: Relation E-ρ_{app} considering the vector of central HU - Method nPS

The FE simulations were performed using this software: *Abaqus* (v13, Simulia, Dassault Systèmes, Rhode Island, U.S.).

2.3 FE analysis

The aim of the simulation is to reproduce a sideways fall condition, the most frequent cause of a femur fracture in the elderly person [53]. For the proximal femurs the neutral configuration was investigated: the reference configuration was obtained by aligning the femurs with respect to the anatomical reference system defined by the axes of the neck and shaft.

Following some validated studies [30], [32], [34], [51], to reproduce this condition of fall were applied these boundary conditions:

- the impact load was applied on the trochanter as a distributed force in x direction;
- the head nodes were bounded to the ground by means of spring elements with a $1000\ N/mm$ stiffness along both the load and in-plane orthogonal directions, to have a static displacement;

- the distal nodes of the proximal femur were connected through link elements to a reference node positioned 0.1 mm distally.

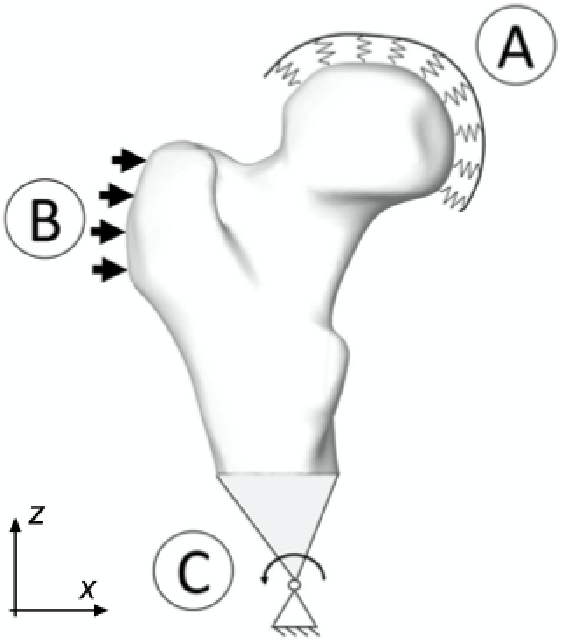

Figure 2.13: scheme of boundary conditions applied for the sideways fall [3]

The choice to use spring elements for the head nodes, depends on acetabular cartilage effect considered [54]. Head nodes usually are bounded, but in this study the use of elastic elements was consistent with the experimental studies in which the cartilage of the head was assumed [33], [50].

While, the choice of how to connect the distal nodes of the models was made to have all translational degrees of freedom fixed [30], [32], [51].

2.4 Post-processing

The finite element analyses strain results were post-processed using a maximum principal strain failure criteria that is largely followed in many studies of fracture prediction that are verified and validated [9], [13], [15], [30], [55], [56]. The principal strains are the variables of interest and the limits values until the strain failure are at 1.04% for the compressive strains and at 0.74% for tensile strains [57]. For each mesh elements, the ratios of the compressive strains (ε_1) and of the tensile strains (ε_3) divided by the corresponding elastic strain limit were calculated. The principal strains were extracted at the centroid; following a validated procedure [15], [30] a Risk Factor (RF) was calculated at each mesh element in this way:

$$RF = \frac{\varepsilon_{max}}{\varepsilon_{lim}}$$

$$\text{Where } \varepsilon_{max} = \max\left(|\varepsilon_1|, \varepsilon_3\right)$$

ε_{max}: is the selected predominant tensile or compressive principal strain;

ε_{lim}: represents the compressive or tensile limit value [53]:

- ε_{lim} *in tension*= 00074;
- ε_{lim} *in compression*= 0.0104.

During sideways falls proximal femur fractures initiate and propagate from the external cortex [15], [30], [48], for that reason only superficial elements were concerned. The FE-estimated failure load was determined scaling the load until one node (failed node) reached RF=1 and the beginning of fracture is considered when the number of contiguous elements in the superolateral cortex with a RF greater than one exceeded the 0.3% of the total surface elements, this percentage corresponds approximately at 40 contiguous mesh elements [30]. Specifically, the elements are recognized contiguous when the distance between their centroids was lower than 1.5 mm.

Two different fracture risk predictors from RF were calculated: the Femoral Strength (FS) and the Risk Factor Index (RFI). These predictors were computed with the femur in the neutral orientation.

The FS, is the minimum force that causes the beginning of bone fracture. This indicator was estimated applying an impact load that follow a ramp function with 100 increment steps, where at the last increment the impact load is of 20000 N, for each load-step the RF was extracted for the cortex elements.

Instead, the RFI indicators is the highest RF found in the bone external cortex with a patient-specific impact load applied with a mass-spring-dumper system. Hence , this indicator depends on mass and height of patients.

To define subject-specific values of the load applied at the trochanter was implemented, on *Simulink* (*MATLAB r2018b*), an equivalent one degree-of-freedom mass-spring-damper dynamic system as reported in Figure 2.14. The impact force onto the greater trochanter is the key factor for predicting fracture risk [58].

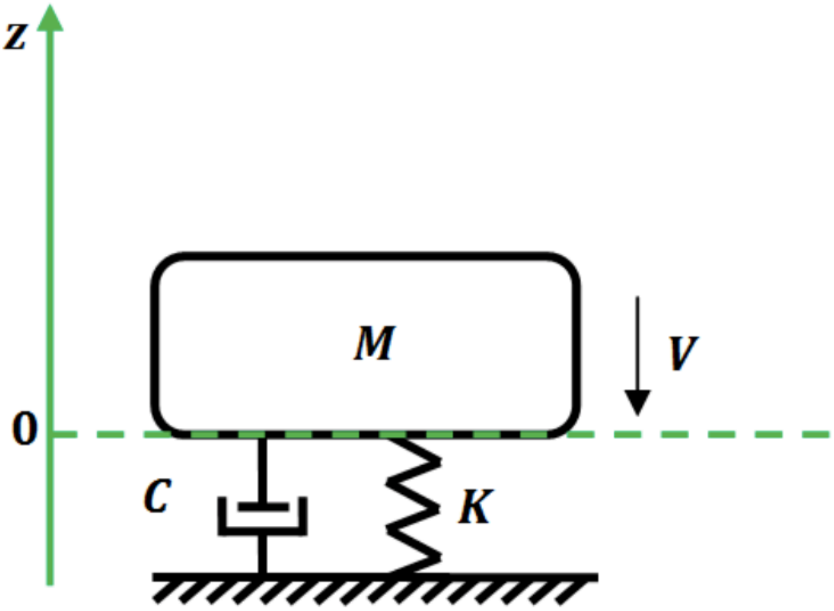

Figure 2.14: mass-spring-damper system [58]

In the dynamic system, the mass value was assigned specifically to each patient and it moves in the vertical direction with velocity (V) prior to impact; the spring (K) and damper (C) represents the effects of the soft tissue and were taken constant in according to previous studies [58]–[60] about trochanteric tissues.

The values adopted in the present study for the spring and damper are selected from experimental studies [58], [60], [61] on the cadavers of elderly individuals (65 ÷ 85 years), specifically the value of stiffness assumed is of 30 $\frac{kN}{m}$, while the value of damping is of 300 $\frac{Ns}{m}$.

Using a one degree-of-freedom impact model, this force is determined by the impact velocity of the hip [62]. To determine impact velocity and effective mass, three different paradigms of increasing complexity were used in literature [62]:

1) a falling point mass or a rigid bar pivoting at its base;

2) two-link models considering of the leg as segment and a torso;
3) three-link models including a knee.

The total mechanical energy of each model before falling was equated to the total mechanical energy just prior to impact in order to estimate the hip impact velocity.

In the present study the body was simplistically adopted as a two-link model [62]: it consists of two slender bars where legs and trunk are considered as two uniform slender bars connected with a frictionless hinge located at the hip, where the bars were chosen to be equal in length, but not in mass.

The impact velocity just before the impact resulted in 2.72 $\sqrt{h}$ [62].

Where h is the total body height in meters.

The average impact velocity was calculated and its value is of 3.39 m/s, with a standard deviation of 0.084 m/s.

This result was achieved employing energy conservation and this two configuration: "*vertical Jack-knife*" fall, where the trunk is vertical just prior to impact, and its variation the "*45 degrees Jack-knife*", that assumes that the trunk angle (defined as the angle between the trunk and the vertical) is 45 degrees just before impact occurs. From the dynamic load output obtained by *Simulink*, the value of the first peak was identified as the impact load to be applied on greater trochanter surface for the RFI extraction.

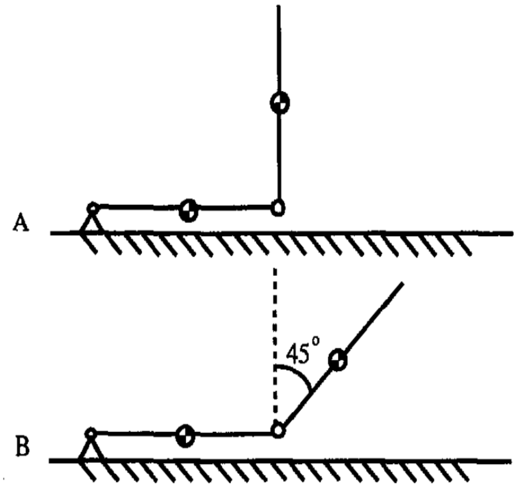

Figure 2.15: (A) vertical Jack-knife model: the trunk is vertical at Impact.
(B) 45-degree Jack- knife model: the trunk is at 45 degrees to the vertical [62].

Three different risk levels were defined according to the obtained RF values:

- Low: $1 < RF < 2$
- Medium: $2 < RF < 3$
- High: $RF > 3$

The principal strains and the RF values derived with the two methods were compared in order to verify the prediction of the tools treated. Specifically, firstly errors about strains and RF at the last load-step of the ramp impact load were computed with respect to the output obtained with the variables of *Method PS* and successfully the outcomes of the two analogous models with different calibration methods were compared in order to evaluate the prediction of fracture risks.

CHAPTER 3

RESULTS and DISCUSSION

3.1 Relative errors evaluation for element-principal strains and RF values

In order to compare the outcomes obtained from the two methods, the element-specific principal strains and RF values were compared and relative errors computed. In the following figures are reported: the comparison between the RF values of both methods for each patient (Figure 3.1), the histograms of subjects with the relative errors about RF (Figure 3.2) and 28 patient-specific models with the errors distribution on the geometry (Figure 3.3 and Figure 3.4).

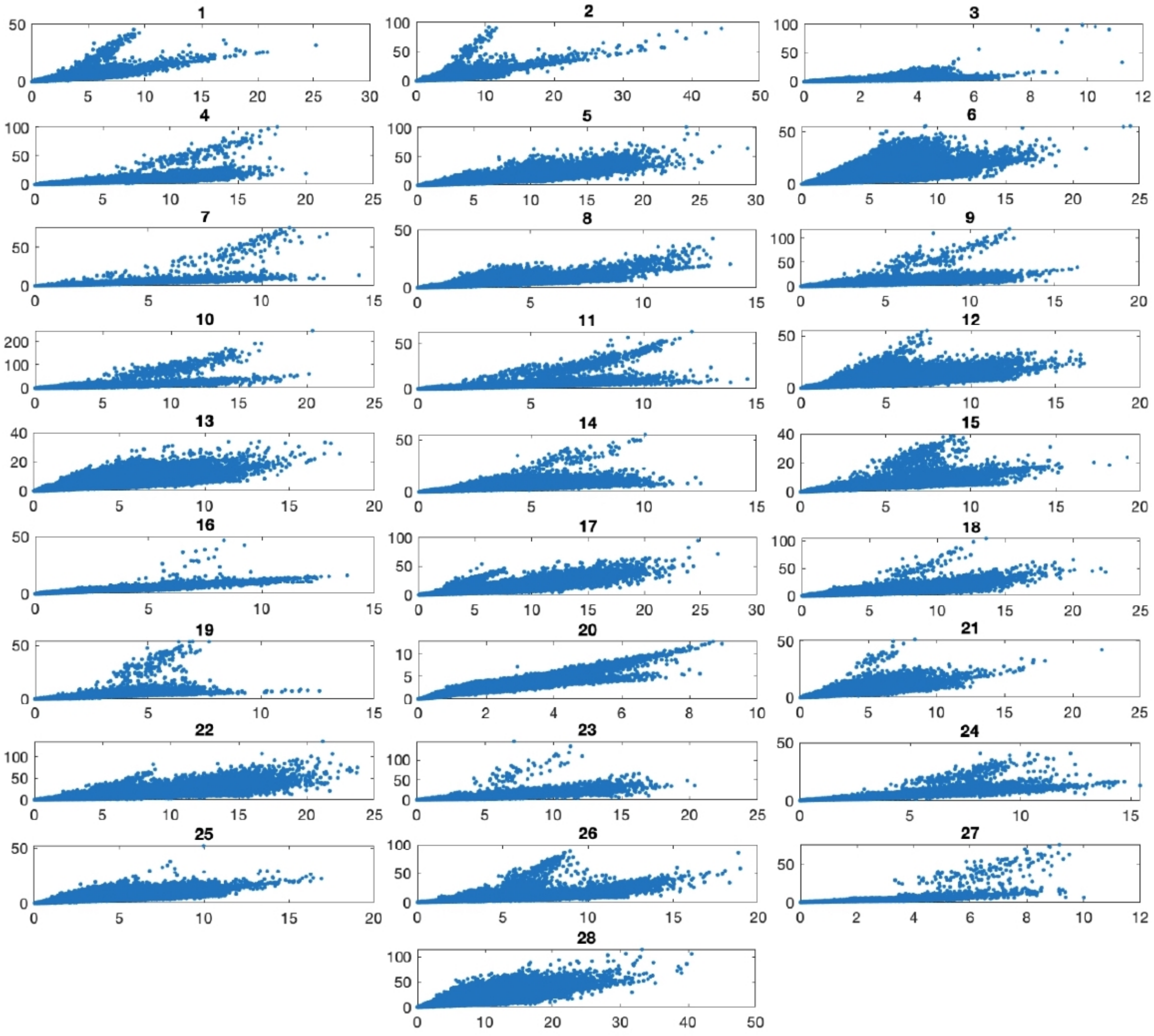

Figure 3.1: Comparison between RF of Methods PS (y-axis) and RF of Methods nPS (x-axis)

As far as principal strains are concerned, the mean relative error considering the patient-specific averages ones is of 25.13% for the compressive principal strain, 24.01% for the tensile one, while the maximum value among the averages ones for each patient was of 33.03% for compressive principal strain and of 31.55% for the tensile one.

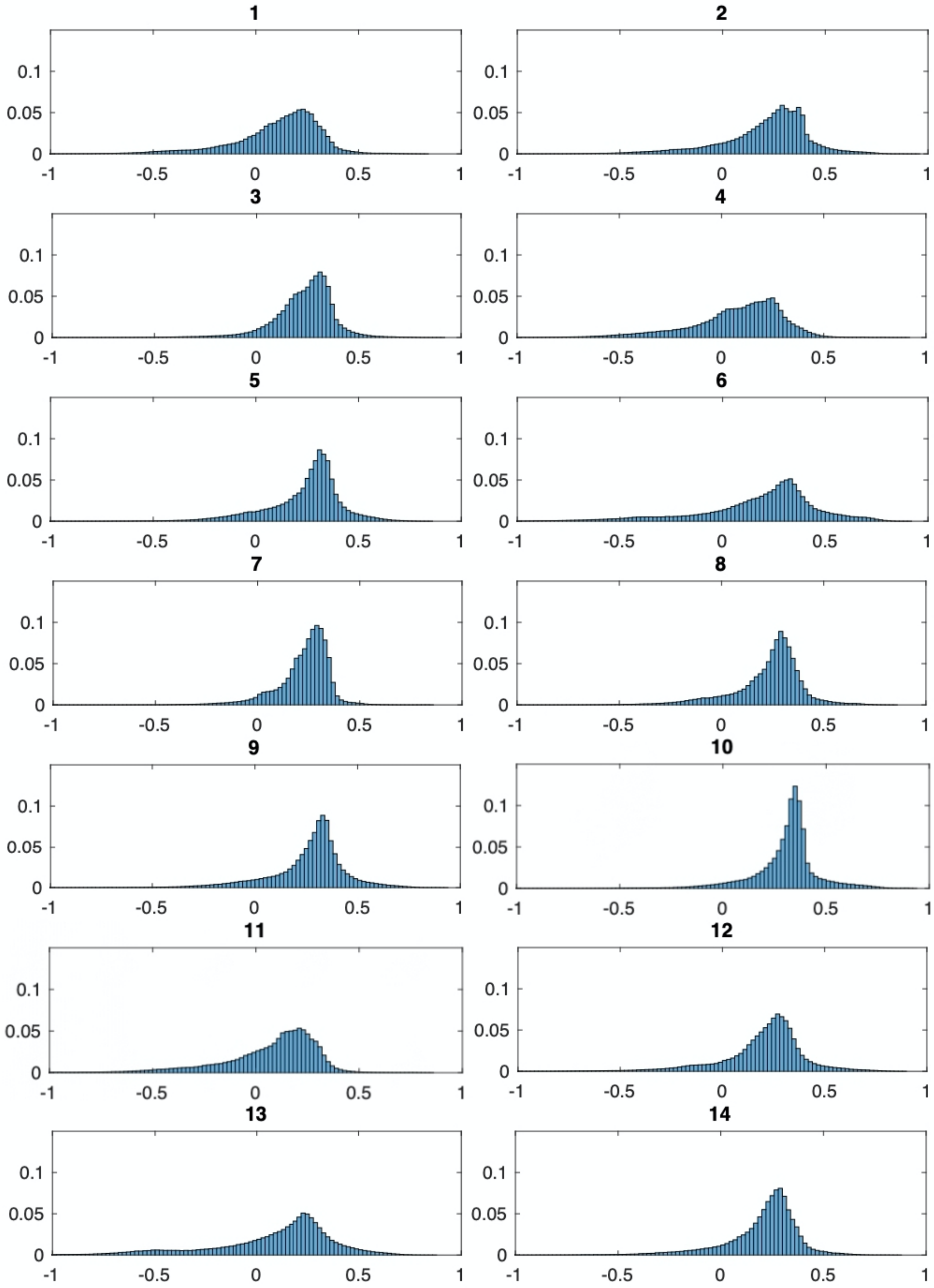

Figure 3.2.1: Histograms of the relative errors from Patient 1 to Patient 14: relative errors (x-axis) and relative frequency (y-axis)

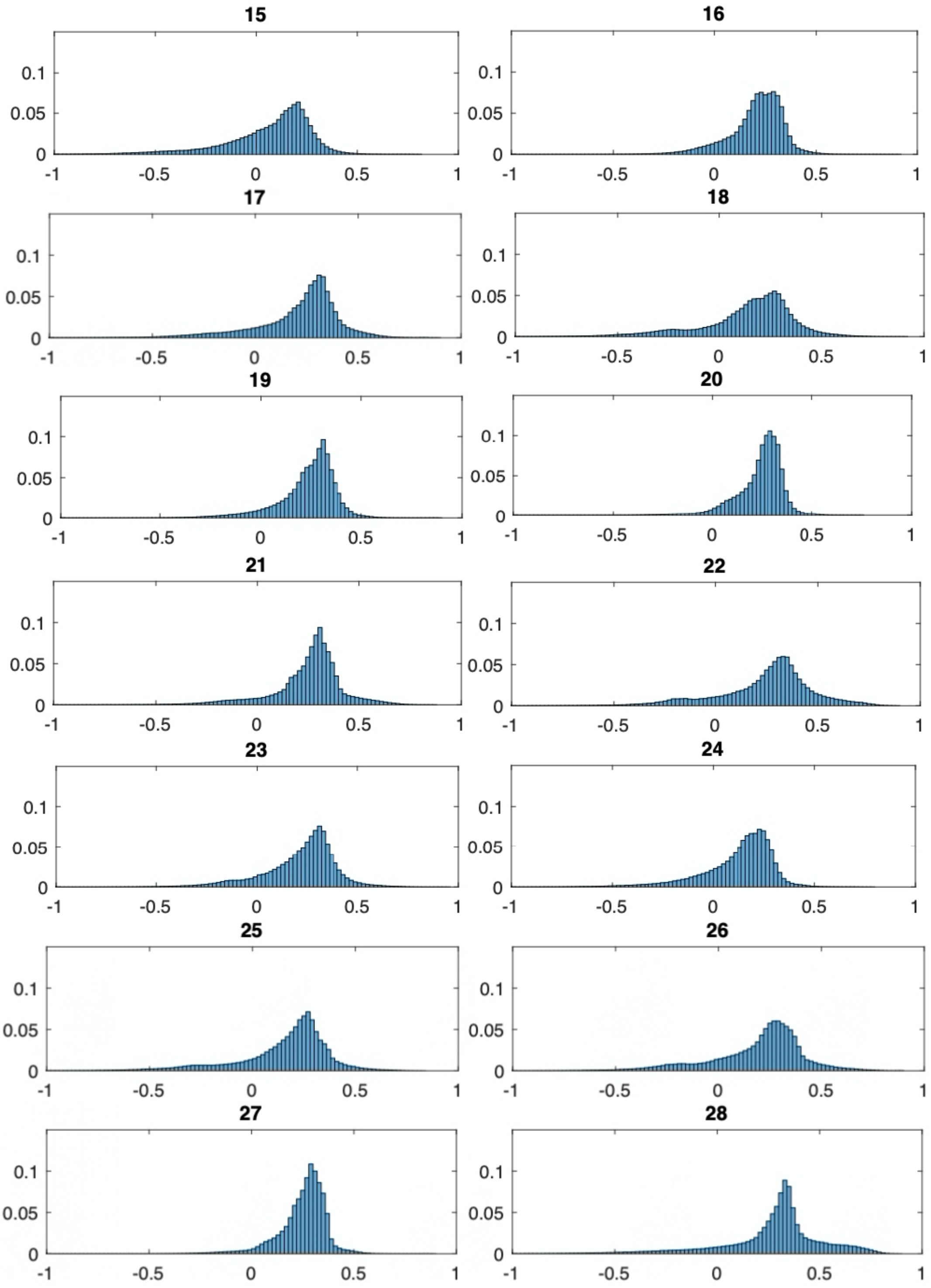

Figure 3.2.2: Histograms of the relative errors from Patient 15 to Patient 28: relative errors (x-axis) and relative frequency (y-axis)

For the RF the relative errors are settled at 25.28% considering the mean value and 33.24% considering the maximum of the mean values. Also the maximum relative errors were calculated for each patient, but the corresponding values even exceeded

100%, although the fracture risk indicators turned out to be correlated, as reported in the following subchapter.

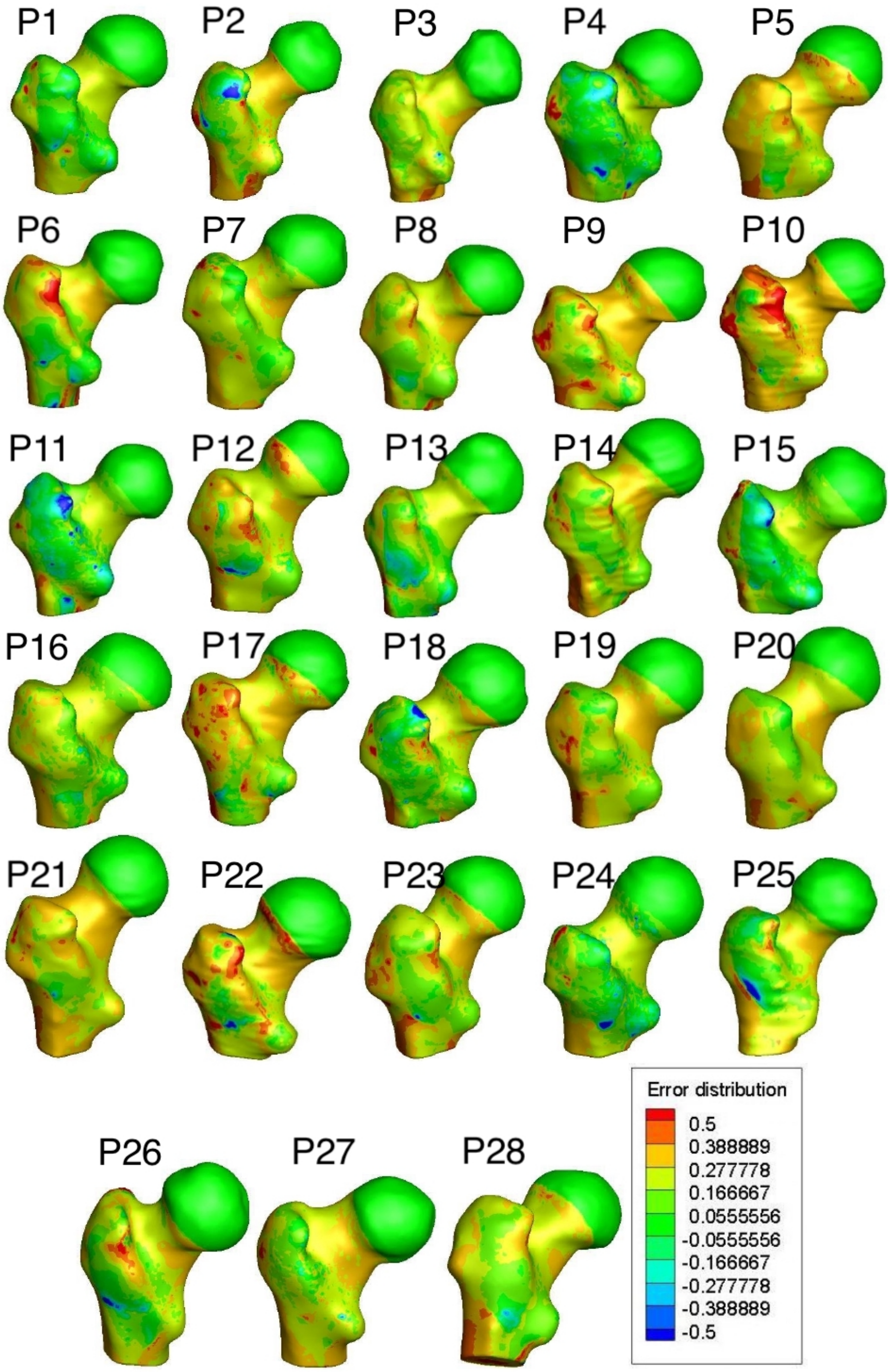

Figure 3.3: Errors distribution on the geometry of models for the 28 patients – Posterior view

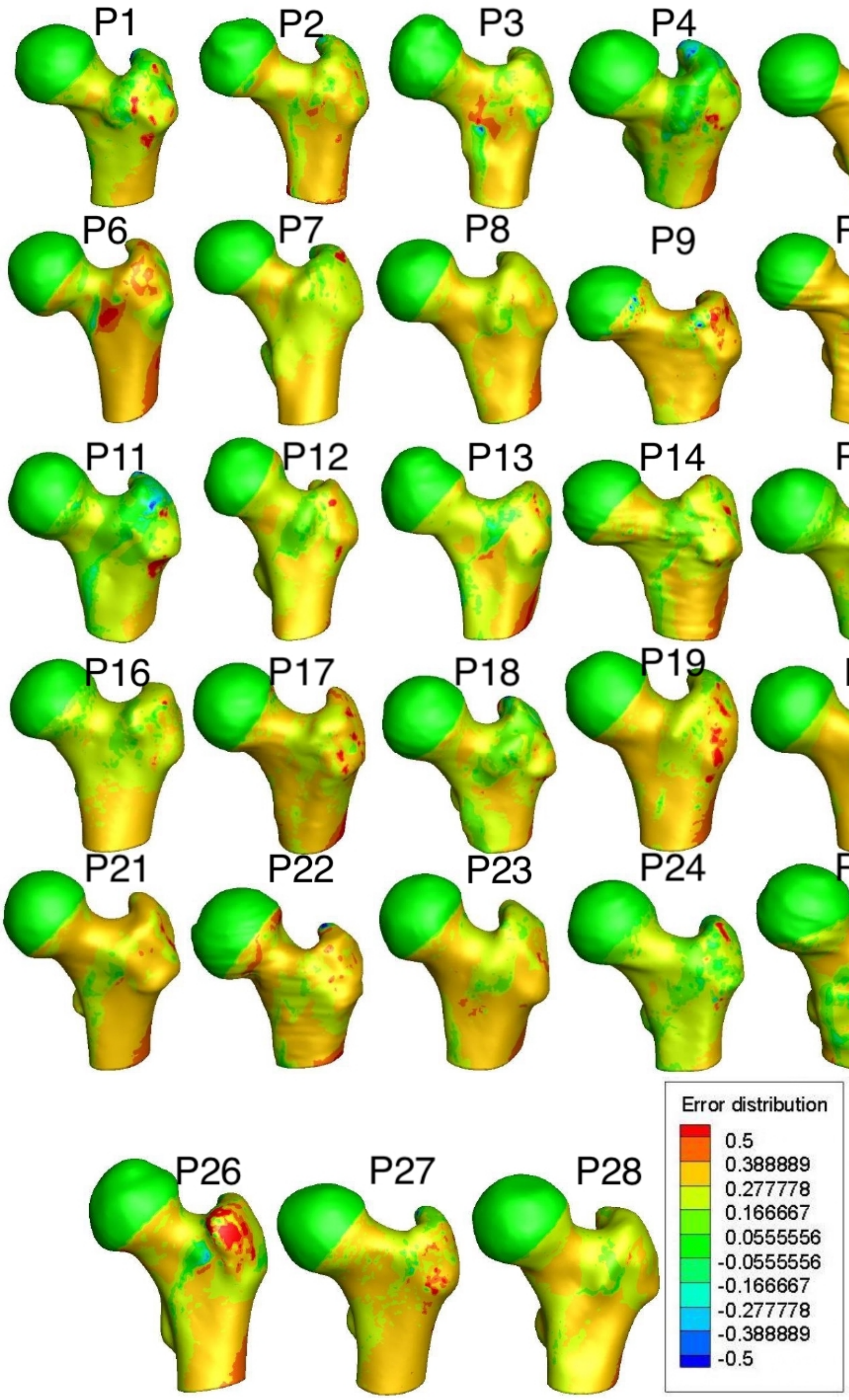

Figure 3.4: Errors distribution on the geometry of models for the 28 patients – Anterior view

Basically, the mean relative error considering the patient-specific average errors values are between 25% and 26%, as highlighted from the histograms (Figure 3.2) and from the “yellow” areas on the geometry that are the most common (Figures 3.3 and 3.4). The errors have an homogeneous distribution: the greater errors are shown at the great trochanter and at lateral femur zone, the lesser errors are at the mean errors are distributed on the neck and shaft femoral. Finally, there are only three subjects (*Patient 8, Patient 16* and *Patient 20*) with a lower error distribution.

3.2 Evaluation of RFI and FS indicators

The of the two methods were compared and turned out to be significantly correlated. The RFI and FS indicators obtained with *Method nPS* have a greater correlation ($R = 0.82$ and $p < 0.0001$) (Figure 3.6) than the same indicators of the *Method PS* ($R = 0.59$ and $p < 0.0001$) (Figure 3.5).

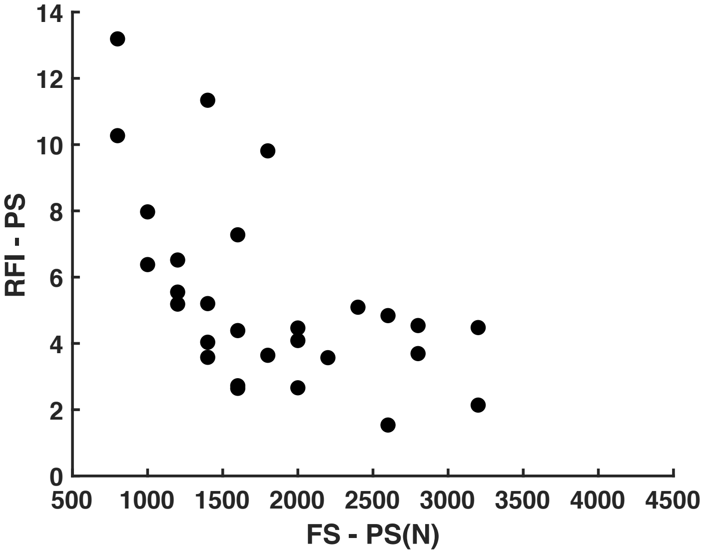

Figure 3.5: Comparison between RFI and FS values for the 28 patients – Methods PS

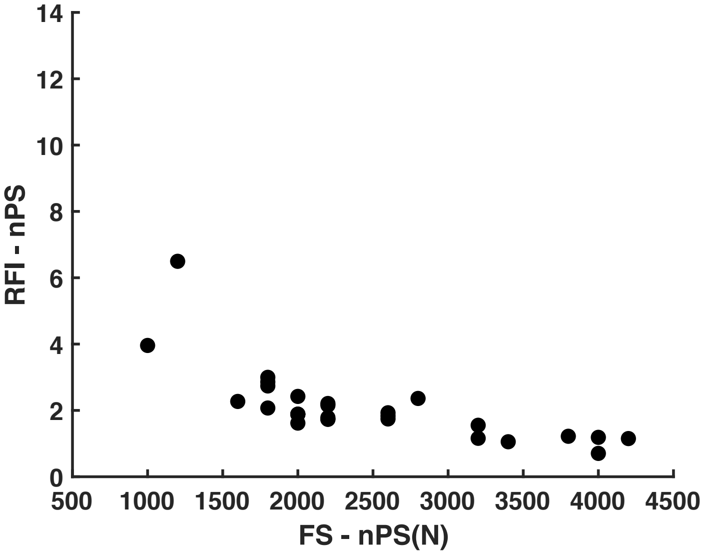

Figure 3.6: Comparison between RFI and FS values for the 28 patients – Methods nPS

The indicators are correlated, although the RFI values were obtained with a patient-specific impact load that is depending on patients mass and height values. To analyze the two different methods the same indicators were compared, as shown in Figure 3.7 and Figure 3.8. The RFI values show a correlation with $R = 0.43$ and $p < 0.02$, while FS values turned out to be more correlated: $R = 0.93$ and $p < 0.00001$.

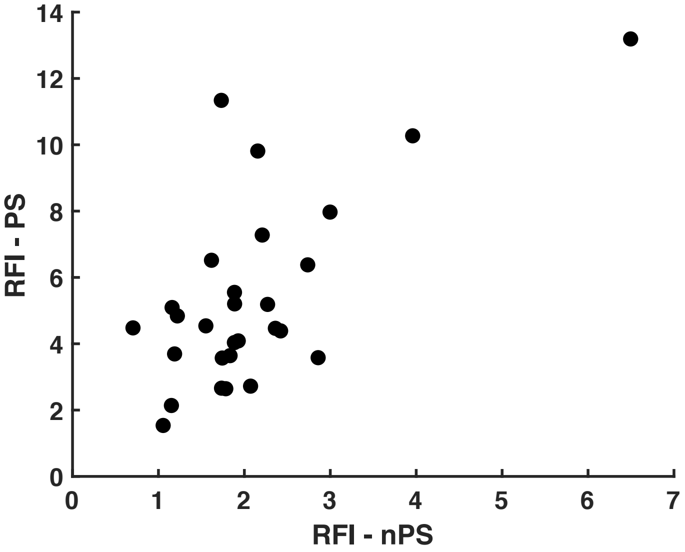

Figure 3.7: Comparison between RFI and FS values for the 28 patients – Methods PS

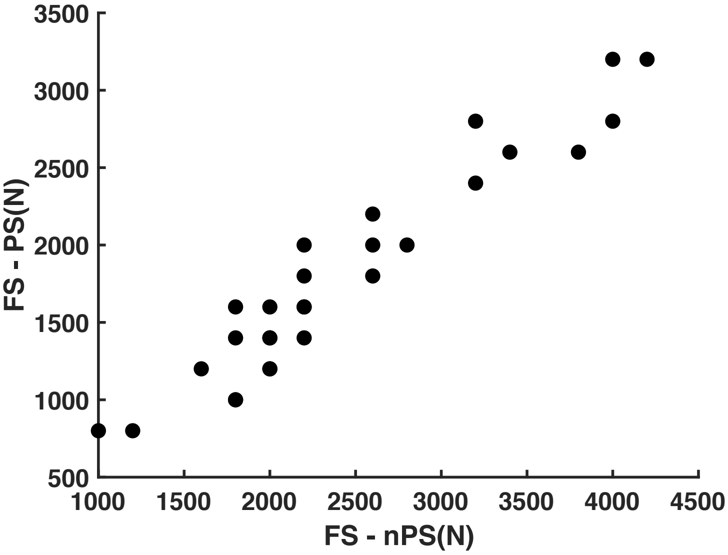

Figure 3.8: Comparison between RFI and FS values for the 28 patients – Methods nPS

In the Figure 3.9 the predictability of RFI and FS for both methods are matched with the T-score values for all patients. The figure ranges highlighted represents the three standard T-score-based criteria to classifies non-osteoporotic and osteoporotic patients. Specifically, osteoporotic patients has a $\mathrm{T-score} < -2.5$, osteopenic patients has a $\mathrm{T-score}$ included between -2.5 and -1, while healthy subjects have a $\mathrm{T-score} > -1$.

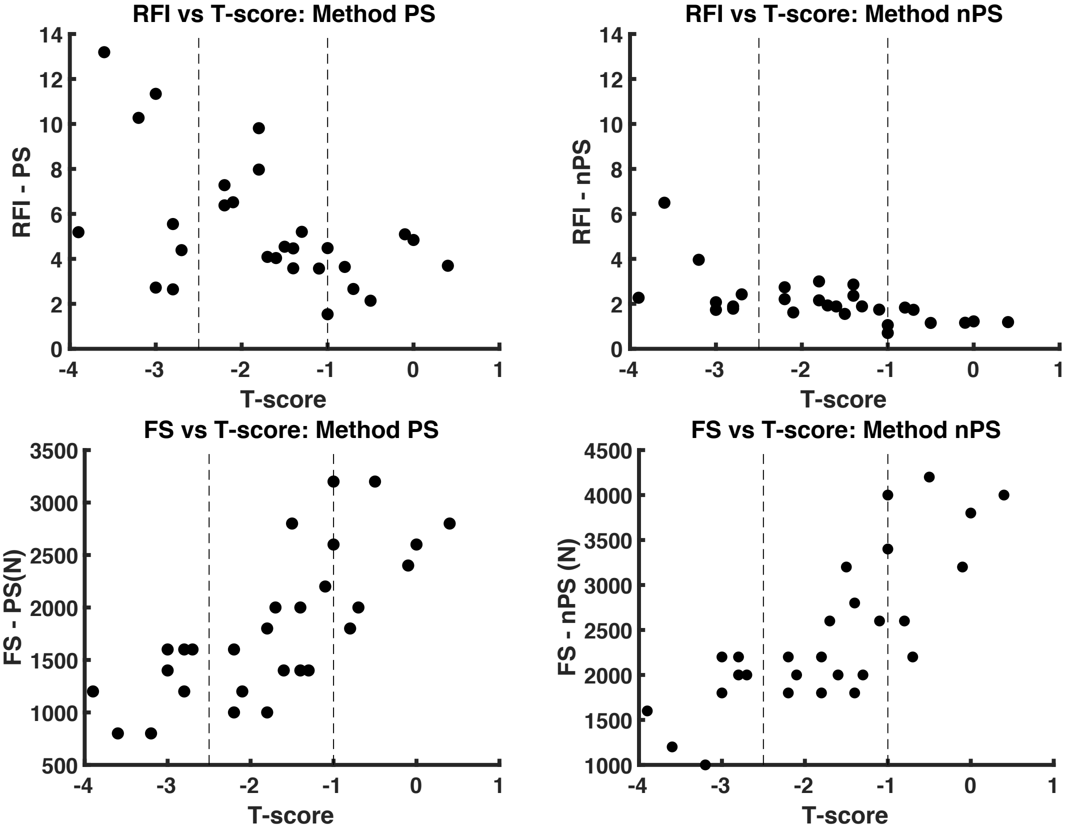

Figure 3.9: Comparison RFI and FS values with T-score of the patients for all method

About the correlation with the T-score, the indicators of *Methods PS* reported: $R = 0.51$ and $p < 0.0001$ for the RFI and $R = 0.74$ and $p < 0.000001$ for the FS. Instead, for *Method nPS* the RFI indicator presents $R = 0.65$ and $p < 0.00001$, while the FS indicator has $R = 0.78$ and $p < 0.00001$. Hence, with the *Method nPS* there is a greater correlation with T-score. Furthermore, despite FS and RFI were both significantly correlated to T-score, a greater number of patients resulted to be at higher risk of fracture according to the *Method PS*. In Figure 3.10 and Figure 3.11 the prediction abilities of the same variable between the methods treated are compared for each patient to better observe the classification of the tools. There are eight osteoporotic subjects and twenty non-osteoporotic subjects in total.

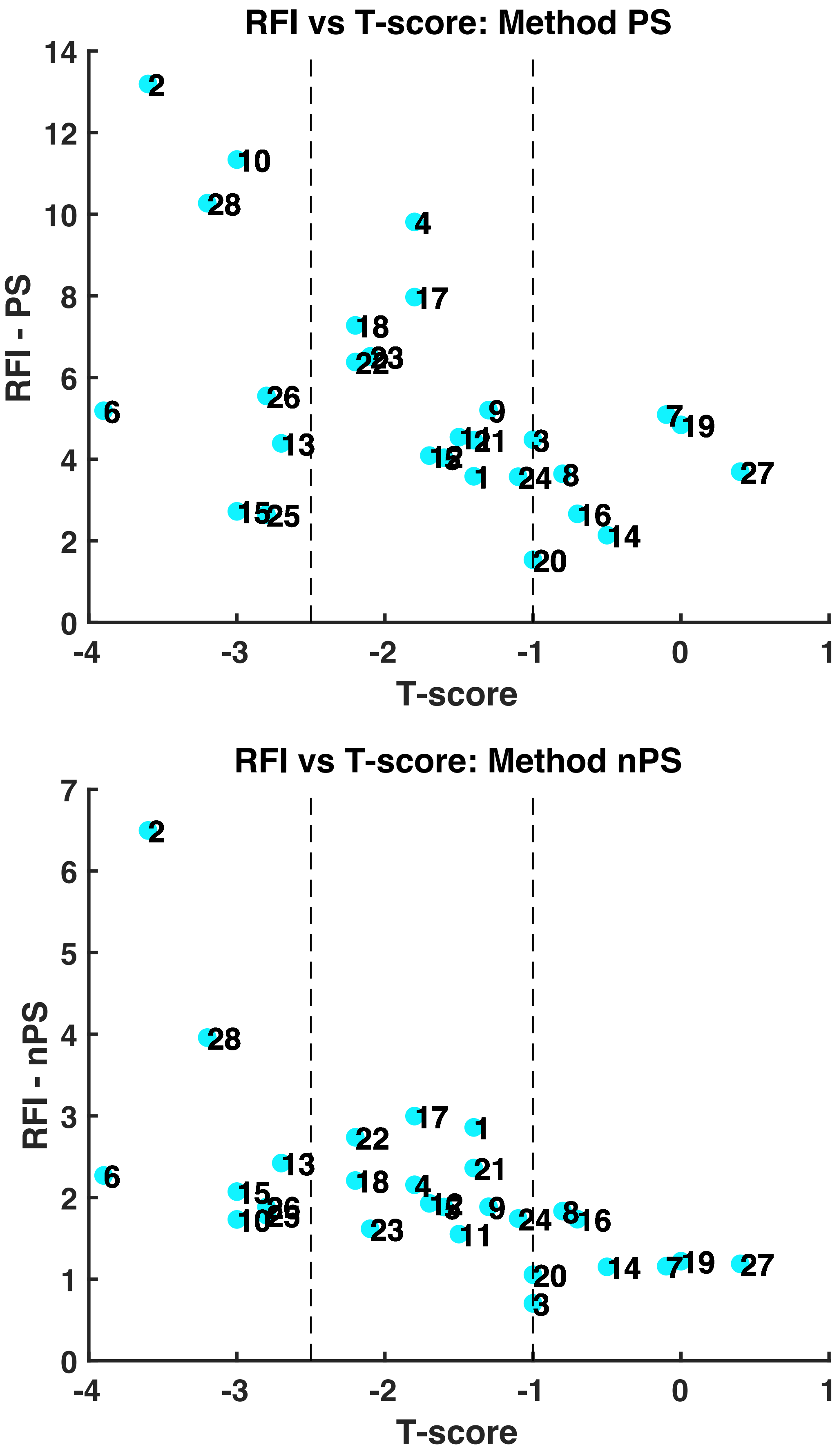

Figure 3.10: Comparison of RFI indicators for both methods with T-score, each patient is represented by a number

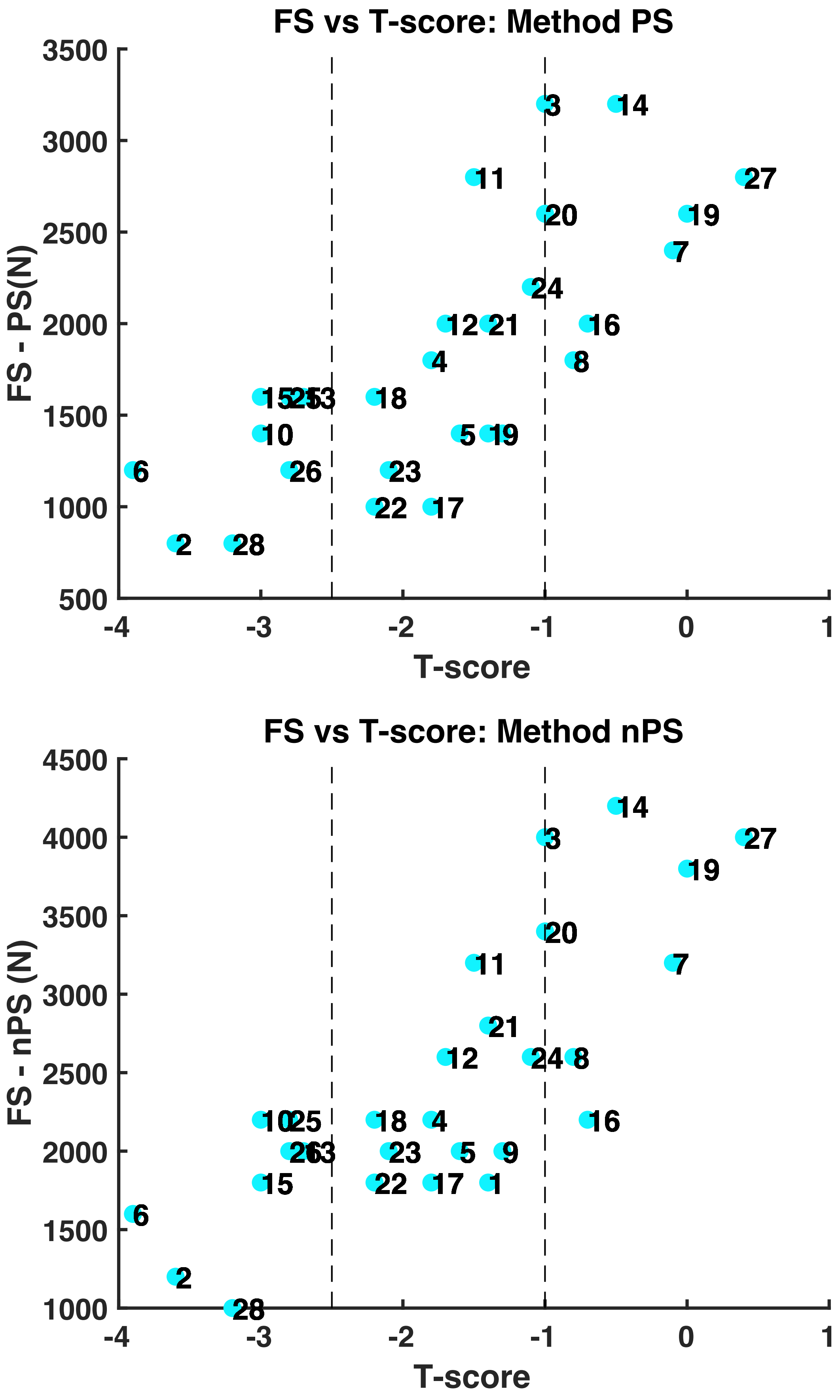

Figure 3.11: Comparison of FS indicators for both methods with T-score, each patient is represented by a number

From the comparison, similarities and differences of classification were highlighted. The RFI indicators: about osteoporotic subjects, both indicators of the two tools classifies *Patient 2* and *Patient 28* at high risk, while *Method PS* identifies also *Patient 10* that appear to be at higher risk of fracture; relative to osteopenic subjects, both indicators considers *Patient 17* at high risk, but the indicator of *Method PS* locates also *Patient 4*, *Patient 18*, *Patient 22 and Patient 23* that appear to be at high risk of fracture; the indicators does not classifies patients with risks about healthy subjects. However, in addition at the larger number of patients classified at a potential fracture level, the RFI-PS shows a better visible stratification of subjects than RFI-nPS. The FS indicators: referring to osteoporotic subjects, both FS identifies all eight osteoporotic patients at high risk of fracture; while for osteopenic subjects, the FS variable of *Method PS* classifies three more subjects that could have a fracture than *Method nPS*: *Patient 12*, *Patient 21* and *Patient 24,* while *Patient 1, Patient 4, Patient 5, Patient 9, Patient 17, Patient 18, Patient 22* and *Patient 23* were considered at high risk from both FS; finally, as healthy subject, *Patient 16* is shown for both FS indicators with a high risk of fracture but *Method PS* identifies also *Patient 8* that appear to be at the same risk level.

In summary, from *Method PS*, the RFI and FS indicators show one more osteoporotic patients and four more non osteoporotic patients who would appear to be at higher risk respect to *Method nPS*. The results of correlation had anticipated the differences between RFI indicators and FS indicators. In particular, the RFI of *Method PS* shows a better visible classification (as shown in Figure 3.10), in fact, while in the classification of the RFI – nPS the subjects are placed very close to each other, with RFI – PS there is a better differentiation. The RFI indicators appear to be more susceptible to the different assignment of material properties. With the patient-specific calibration, the HU-BMD conversion includes the effects of patient-specific physical factors on the HU values [36].These factors could explain the difference about classification and the better RFI – PS distinction than the RFI - nPS. On the other hand, also the FS indicators show differences about classification but the distribution on the graphs is more homogeneous. To explain the differences of the two indicators it should be remembered how they were defined: the RFI is the highest RF value found with a one degree of freedom mass-spring-damper system, hence depends on the greatest principal strain; while, the FS is the maximum load with which a ramp function generates the fracture, the beginning of the fracture depends on a number of contiguous elements that exceeded the 0.3% of the total external cortex with an RF >1. For FS predictors, in Figure 3.12 the load-steps where the fractures occurred were compared: all the fractures with *Method PS* appear at lower impact loads than the *Method nPS*. Moreover, the subjects classified as osteoporotic by the T-score are all identified with a high risk of fracture from the FS indicators, but these results are better highlighted with FS – PS due to lower FS values that identifies the patients, while the RFI does not identifies all osteoporotic patients at high risk. Unfortunately, the lack of follow-up information did not allow the validation of the obtained results, but in the future the same comparison will be applied to retrospective cohorts with follow-up information included to fully assed the power of the proposed methodology.

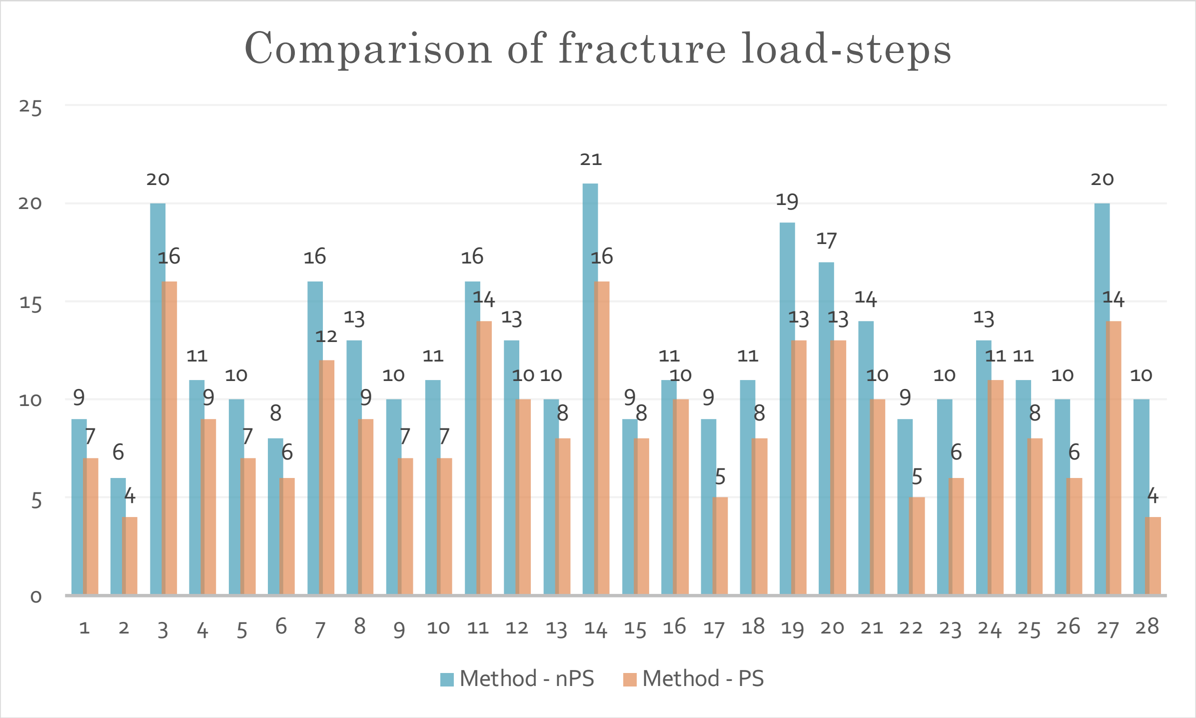

Figure 3.12: Comparison between Method PS and Method nPS of the load-steps when fractures occurred

Anyway, the impossibility to apply the gold standard at the calibration and with the employing of the pseudo-calibration, surely error sources have been introduced, included within the FE models, that influenced the materials assignment and the estimation of strains. Although the good results of this study, another purpose is to develop and to follow each step of the gold standard based on CT-FEA.

Finally, in the following figures (Figure 3.13 and Figure 3.14) the superficial distribution of the RF values are shown for the 28 models at the timestep which the fractures occurred for *Method PS*. As can be seen from the images, the highest RF values are concentrated behind the greater trochanter, but this is the area where the loads have been applied, in fact, for this reason this site was not considered for the definition of RFI and FS predictors. Other important areas of failure are highlighted on the femoral necks. In all figures, the cell-centered variables are interpolated at the nodes and the RF values under the 90^{th} percentile are discarded. The considered percentile of the RF values from *Method PS* (0.55) is greater than the value of the other approach evaluated (0.41). As can be expected from the values of the 90^{th} percentiles, the "yellow" areas of the models of *Method nPS* are greater than the same respective areas of the models of *Method PS*, but this last reports a greater "red" and "black" areas, as can be seen on the femur models of *Patient 1*, *Patient 4*, *Patient 9*, *Patient 11*, *Patient 19*, *Patient 24* and *Patient 26*. In addition, in Figure 3.13 and Figure 3.14 the failed arear are highlighted with arrows.

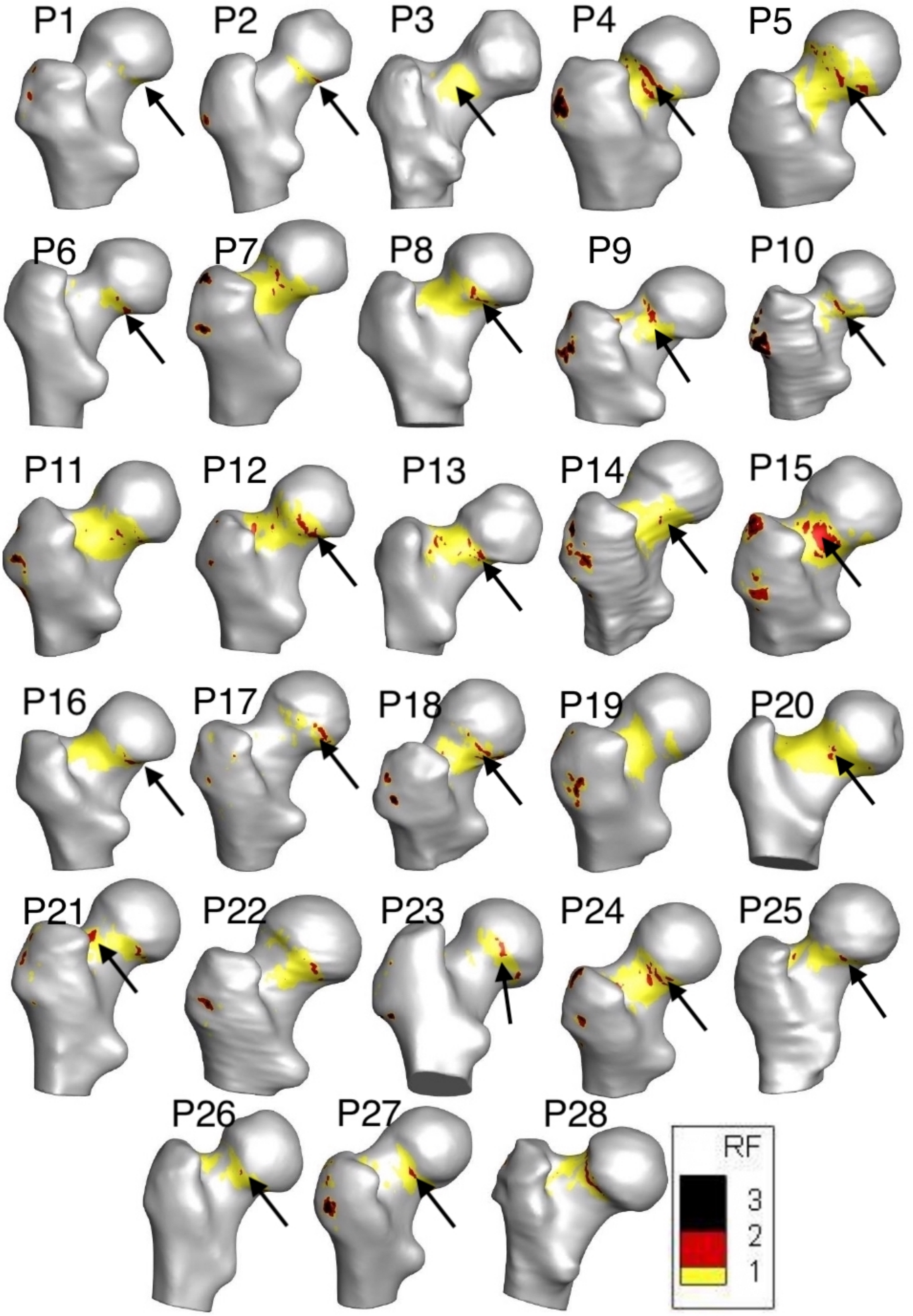

Figure 3.13: Superficial RF distribution for the 28 patient-specific models for Method PS. The failed areas are highlighted with arrows (Posterior view)

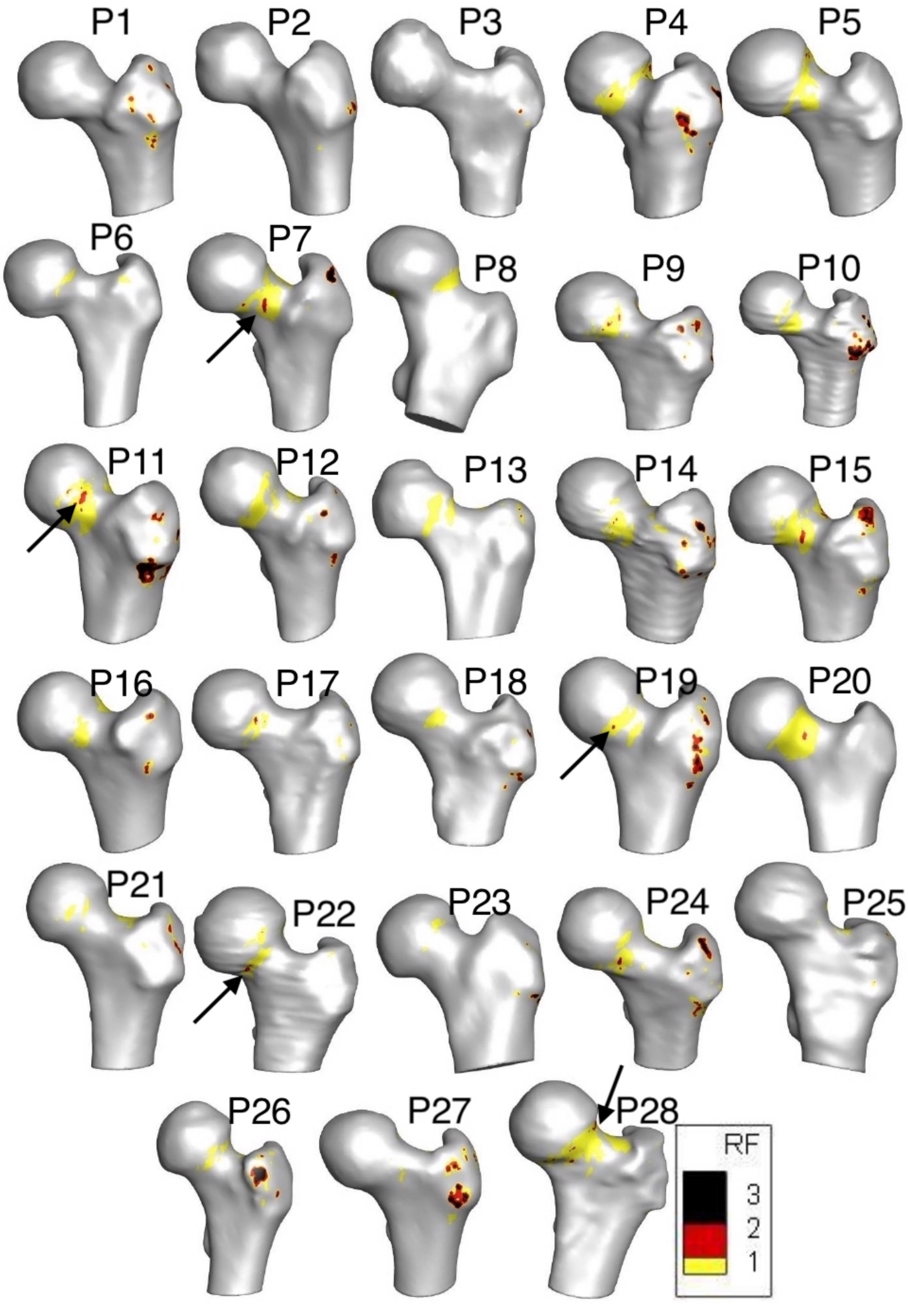

Figure 3.14: Superficial RF distribution for the 28 patient-specific models for Method PS. The failed areas are highlighted with arrows. (Anterior view)

CHAPTER 4

CONCLUSIONS

The low sensitivity of the T-score about the prediction of hip fractures caused by osteoporosis has led to the development of CT images Finite Element Analysis. The aim of the present thesis work is to propose an alternative method to a common problem that occurs in the case of CT-FEA: the absence of a calibration phantom. Hence, a patient-specific phantom-less strategy was implemented following a study presented in the literature. For each patient, a calibration function to convert HU values to local bone mineral density based on air, fat and muscle as calibration references was obtained and applying appropriate physic relationships the material properties were mapped into models. After simulating a sideways fall the principal strains on the superficial elements of the models were extracted and two different predictors were evaluated with a post-processing phase. To evaluate the performance of this methodology the outcomes were compared with analogous models obtained with a different calibration method that is not patient specific. Important differences about the principal strains on the surface were shown comparing the outcomes and computing the relative errors. Moreover, the predictors of the two methods were compared with the T-scores reporting the differences regarding the classification of patients who appear to be at a higher risk of fracture, where the patient-specific method reported a visible better classification. Specifically, with the method patient-specific a greater number of evaluated subjects appear to be at higher risk of fracture. Furthermore, the RFIs have been shown to be more susceptible at material assignment, in fact, these predictors have been shown greater differences about classification than the FS predictors between the two strategies. Hence, the present study found that the patient-specific calibration improves qualitatively the classification of subjects with a risk of hip fracture. However, this thesis can be defined as an exploratory study, due to the lack of follow-up information did not allow the validation of the results obtained. In fact, the next step will be to apply the same methodologies to a retrospective cohort with follow-up information available to fully evaluate the potential of the proposed strategy.

REFERENCES

[1] T. Sozen, L. Ozisik, e N. Calik Basaran, «An overview and management of osteoporosis», *Eur. J. Rheumatol.*, vol. 4, n. 1, pagg. 46–56, mar. 2017, doi: 10.5152/eurjrheum.2016.048.

[2] A. E. Razi e S. H. Hershman, A c. di, *Vertebral Compression Fractures in Osteoporotic and Pathologic Bone: A Clinical Guide to Diagnosis and Management*. Cham: Springer International Publishing, 2020.

[3] A. Aldieri, «Fracture Risk of the Proximal Femur in Osteoporosis: a Closer Look at the Role of Geometry», pag. 170.

[4] M. A. Clynes, N. C. Harvey, E. M. Curtis, N. R. Fuggle, E. M. Dennison, e C. Cooper, «The epidemiology of osteoporosis», vol. 00, pag. 13, 2020.

[5] A. Aldieri *et al.*, «Osteoporotic Hip Fracture Prediction: Is T-Score-Based Criterion Enough? A Hip Structural Analysis-Based Model», *J. Biomech. Eng.*, vol. 140, n. 11, pag. 111004, nov. 2018, doi: 10.1115/1.4040586.

[6] J. H. Keyak *et al.*, «Male–female differences in the association between incident hip fracture and proximal femoral strength: A finite element analysis study», *Bone*, vol. 48, n. 6, pagg. 1239–1245, giu. 2011, doi: 10.1016/j.bone.2011.03.682.

[7] DIREZIONE GENERALE DELLA PROGRAMMAZIONE SANITARIA, DEI LIVELLI DI ASSISTENZA E DEI PRINCIPI ETICI DI SISTEMA, «Individuazione dei criteri di Accesso alla Densitometria Ossea». Ministero della salute-Dipartimento della qualità, feb. 2005.

[8] K. E. Ackerman *et al.*, «Hip Structural Analysis in Adolescent and Young Adult Oligoamenorrheic and Eumenorrheic Athletes and Nonathletes», *J. Clin. Endocrinol. Metab.*, vol. 98, n. 4, pagg. 1742–1749, apr. 2013, doi: 10.1210/jc.2013-1006.

[9] M. Qasim *et al.*, «Patient-specific finite element estimated femur strength as a predictor of the risk of hip fracture: the effect of methodological determinants», *Osteoporos. Int.*, vol. 27, n. 9, pagg. 2815–2822, set. 2016, doi: 10.1007/s00198-016-3597-4.

[10] T. M. Keaveny *et al.*, «Biomechanical Computed Tomography analysis (BCT) for clinical assessment of osteoporosis», *Osteoporos. Int.*, vol. 31, n. 6, pagg. 1025–1048, giu. 2020, doi: 10.1007/s00198-020-05384-2.

[11] Y. Katz, G. Dahan, J. Sosna, I. Shelef, E. Cherniavsky, e Z. Yosibash, «Scanner influence on the mechanical response of QCT-based finite element analysis of long bones», *J. Biomech.*, vol. 86, pagg. 149–159, mar. 2019, doi: 10.1016/j.jbiomech.2019.01.049.

[12] F. Johannesdottir, B. Allaire, e M. L. Bouxsein, «Fracture Prediction by Computed Tomography and Finite Element Analysis: Current and Future Perspectives», *Curr. Osteoporos. Rep.*, vol. 16, n. 4, pagg. 411–422, ago. 2018, doi: 10.1007/s11914-018-0450-z.

[13] M. Bessho, I. Ohnishi, J. Matsuyama, T. Matsumoto, K. Imai, e K. Nakamura, «Prediction of strength and strain of the proximal femur by a CT-based finite element method», *J. Biomech.*, vol. 40, n. 8, pagg. 1745–1753, gen. 2007, doi: 10.1016/j.jbiomech.2006.08.003.

[14] J. H. Keyak, T. S. Kaneko, J. Tehranzadeh, e H. B. Skinner, «Predicting Proximal Femoral

Strength Using Structural Engineering Models»:, *Clin. Orthop.*, vol. NA;, n. 437, pagg. 219–228, ago. 2005, doi: 10.1097/01.blo.0000164400.37905.22.

[15] E. Schileo, F. Taddei, A. Malandrino, L. Cristofolini, e M. Viceconti, «Subject-specific finite element models can accurately predict strain levels in long bones», *J. Biomech.*, vol. 40, n. 13, pagg. 2982–2989, gen. 2007, doi: 10.1016/j.jbiomech.2007.02.010.

[16] N. Trabelsi e Z. Yosibash, «Patient-Specific Finite-Element Analyses of the Proximal Femur with Orthotropic Material Properties Validated by Experiments», *J. Biomech. Eng.*, vol. 133, n. 6, pag. 061001, giu. 2011, doi: 10.1115/1.4004180.

[17] P. Gargiulo *et al.*, «Anthropometry of Human Muscle Using Segmentation Techniques and 3D Modelling: Applications to Lower Motor Neuron Denervated Muscle in Spinal Cord Injury», in *Handbook of Anthropometry*, V. R. Preedy, A c. di New York, NY: Springer New York, 2012, pagg. 323–354.

[18] Þ. Pétursson, B. Magnússon, B. Helgason, G. Halldórsson, J. Tribel, e P. Gargiulo, «Bone and muscle assessment in patients undergoing total hip arthroplasty using HU based analysis», pag. 6.

[19] T. Vrtovec, B. Likar, e F. Pernuš, «Automated curved planar reformation of 3D spine images», *Phys. Med. Biol.*, vol. 50, n. 19, pagg. 4527–4540, ott. 2005, doi: 10.1088/0031-9155/50/19/007.

[20] N. K. Knowles, J. M. Reeves, e L. M. Ferreira, «Quantitative Computed Tomography (QCT) derived Bone Mineral Density (BMD) in finite element studies: a review of the literature», *J. Exp. Orthop.*, vol. 3, n. 1, pag. 36, dic. 2016, doi: 10.1186/s40634-016-0072-2.

[21] M. Ruess, D. Tal, N. Trabelsi, Z. Yosibash, e E. Rank, «The finite cell method for bone simulations: verification and validation», *Biomech. Model. Mechanobiol.*, vol. 11, n. 3–4, pagg. 425–437, mar. 2012, doi: 10.1007/s10237-011-0322-2.

[22] J. H. Keyak e Y. Falkinstein, «Comparison of in situ and in vitro CT scan-based finite element model predictions of proximal femoral fracture load», *Med. Eng. Phys.*, vol. 25, n. 9, pagg. 781–787, nov. 2003, doi: 10.1016/S1350-4533(03)00081-X.

[23] C. M. Les, J. H. Keyak, S. M. Stover, K. T. Taylor, e A. J. Kaneps, «Estimation of material properties in the equine metacarpus with use of quantitative computed tomography», *J. Orthop. Res.*, vol. 12, n. 6, pagg. 822–833, nov. 1994, doi: 10.1002/jor.1100120610.

[24] K. G. Faulkner, C. C. Glüer, S. Grampp, e H. K. Genant, «Cross-calibration of liquid and solid QCT calibration standards: Corrections to the UCSF normative data», *Osteoporos. Int.*, vol. 3, n. 1, pagg. 36–42, gen. 1993, doi: 10.1007/BF01623175.

[25] D. D. Cody, F. J. Hou, G. W. Divine, e D. P. Fyhrie, «Short Term In Vivo Precision of Proximal Femoral Finite Element Modeling», *Ann. Biomed. Eng.*, vol. 28, n. 4, pagg. 408–414, apr. 2000, doi: 10.1114/1.278.

[26] E. Tanck *et al.*, «Pathological fracture prediction in patients with metastatic lesions can be improved with quantitative computed tomography based computer models», *Bone*, vol. 45, n. 4, pagg. 777–783, ott. 2009, doi: 10.1016/j.bone.2009.06.009.

[27] E. F. Morgan, H. H. Bayraktar, e T. M. Keaveny, «Trabecular bone modulus–density

relationships depend on anatomic site», *J. Biomech.*, vol. 36, n. 7, pagg. 897–904, lug. 2003, doi: 10.1016/S0021-9290(03)00071-X.

[28] E. Schileo *et al.*, «An accurate estimation of bone density improves the accuracy of subject-specific finite element models», *J. Biomech.*, vol. 41, n. 11, pagg. 2483–2491, ago. 2008, doi: 10.1016/j.jbiomech.2008.05.017.

[29] S. Eberle, M. Göttlinger, e P. Augat, «An investigation to determine if a single validated density–elasticity relationship can be used for subject specific finite element analyses of human long bones», *Med. Eng. Phys.*, vol. 35, n. 7, pagg. 875–883, lug. 2013, doi: 10.1016/j.medengphy.2012.08.022.

[30] E. Schileo, L. Balistreri, L. Grassi, L. Cristofolini, e F. Taddei, «To what extent can linear finite element models of human femora predict failure under stance and fall loading configurations?», *J. Biomech.*, vol. 47, n. 14, pagg. 3531–3538, nov. 2014, doi: 10.1016/j.jbiomech.2014.08.024.

[31] L. Duchemin, D. Mitton, E. Jolivet, V. Bousson, J. D. Laredo, e W. Skalli, «An anatomical subject-specific FE-model for hip fracture load prediction», *Comput. Methods Biomech. Biomed. Engin.*, vol. 11, n. 2, pagg. 105–111, apr. 2008, doi: 10.1080/10255840701535965.

[32] D. Dragomir-Daescu *et al.*, «Robust QCT/FEA Models of Proximal Femur Stiffness and Fracture Load During a Sideways Fall on the Hip», *Ann. Biomed. Eng.*, vol. 39, n. 2, pagg. 742–755, feb. 2011, doi: 10.1007/s10439-010-0196-y.

[33] J. E. M. Koivumäki *et al.*, «Ct-based finite element models can be used to estimate experimentally measured failure loads in the proximal femur», *Bone*, vol. 50, n. 4, pagg. 824–829, apr. 2012, doi: 10.1016/j.bone.2012.01.012.

[34] K. K. Nishiyama, S. Gilchrist, P. Guy, P. Cripton, e S. K. Boyd, «Proximal femur bone strength estimated by a computationally fast finite element analysis in a sideways fall configuration», *J. Biomech.*, vol. 46, n. 7, pagg. 1231–1236, apr. 2013, doi: 10.1016/j.jbiomech.2013.02.025.

[35] E. Dall'Ara, D. Pahr, P. Varga, F. Kainberger, e P. Zysset, «QCT-based finite element models predict human vertebral strength in vitro significantly better than simulated DEXA», *Osteoporos. Int.*, vol. 23, n. 2, pagg. 563–572, feb. 2012, doi: 10.1007/s00198-011-1568-3.

[36] Y. H. Lee, J. J. Kim, e I. G. Jang, «Patient-Specific Phantomless Estimation of Bone Mineral Density and Its Effects on Finite Element Analysis Results: A Feasibility Study», *Comput. Math. Methods Med.*, vol. 2019, pagg. 1–10, gen. 2019, doi: 10.1155/2019/4102410.

[37] D. C. Lee, P. F. Hoffmann, D. L. Kopperdahl, e T. M. Keaveny, «Phantomless calibration of CT scans for measurement of BMD and bone strength—Inter-operator reanalysis precision», *Bone*, vol. 103, pagg. 325–333, ott. 2017, doi: 10.1016/j.bone.2017.07.029.

[38] Cristopher E. Cann e Harry K. Genant, «Precise Measurement of Vertebral Mineral Content Using Computed Tomography», ago. 1980.

[39] M. J. Budoff *et al.*, «Measurement of Phantomless Thoracic Bone Mineral Density on Coronary Artery Calcium CT Scans Acquired with Various CT Scanner Models», *Radiology*, vol. 267, n. 3, pagg. 830–836, giu. 2013, doi: 10.1148/radiol.13111987.

[40] P. J. Pickhardt *et al.*, «Simultaneous screening for osteoporosis at CT colonography: Bone

mineral density assessment using MDCT attenuation techniques compared with the DXA reference standard», *J. Bone Miner. Res.*, vol. 26, n. 9, pagg. 2194–2203, set. 2011, doi: 10.1002/jbmr.428.

[41] P. J. Pickhardt, B. D. Pooler, T. Lauder, A. M. del Rio, R. J. Bruce, e N. Binkley, «Opportunistic Screening for Osteoporosis Using Abdominal Computed Tomography Scans Obtained for Other Indications», *Ann. Intern. Med.*, vol. 158, n. 8, pag. 588, apr. 2013, doi: 10.7326/0003-4819-158-8-201304160-00003.

[42] F. Eggermont *et al.*, «Can patient-specific finite element models better predict fractures in metastatic bone disease than experienced clinicians?: Towards computational modelling in daily clinical practice», *Bone Jt. Res.*, vol. 7, n. 6, pagg. 430–439, giu. 2018, doi: 10.1302/2046-3758.76.BJR-2017-0325.R2.

[43] F. Eggermont, N. Verdonschot, Y. van der Linden, e E. Tanck, «Calibration with or without phantom for fracture risk prediction in cancer patients with femoral bone metastases using CT-based finite element models», *PLOS ONE*, vol. 14, n. 7, pag. e0220564, lug. 2019, doi: 10.1371/journal.pone.0220564.

[44] C. Winsor *et al.*, «Evaluation of patient tissue selection methods for deriving equivalent density calibration for femoral bone quantitative CT analyses», *Bone*, vol. 143, pag. 115759, feb. 2021, doi: 10.1016/j.bone.2020.115759.

[45] I. Ridzwan, «A Computational Orthopaedic Biomechanics Study of Osteoporotic Hip Fractures», pag. 168.

[46] M. I. Z. Ridzwan *et al.*, «Femoral fracture type can be predicted from femoral structure: A finite element study validated by digital volume correlation experiments: FEMORAL FRACTURE TYPE CAN BE PREDICTED FROM FEMORAL STRUCTURE», *J. Orthop. Res.*, ago. 2017, doi: 10.1002/jor.23669.

[47] J. H. Keyak *et al.*, «Effect of finite element model loading condition on fracture risk assessment in men and women: The AGES-Reykjavik study», *Bone*, vol. 57, n. 1, pagg. 18–29, nov. 2013, doi: 10.1016/j.bone.2013.07.028.

[48] P. M. de Bakker, S. L. Manske, V. Ebacher, T. R. Oxland, P. A. Cripton, e P. Guy, «During sideways falls proximal femur fractures initiate in the superolateral cortex: Evidence from high-speed video of simulated fractures», *J. Biomech.*, vol. 42, n. 12, pagg. 1917–1925, ago. 2009, doi: 10.1016/j.jbiomech.2009.05.001.

[49] A. C. Courtney, E. F. Wachtel, E. R. Myers, e W. C. Hayes, «Effects of loading rate on strength of the proximal femur», *Calcif. Tissue Int.*, vol. 55, n. 1, pagg. 53–58, lug. 1994, doi: 10.1007/BF00310169.

[50] F. Eckstein *et al.*, «Reproducibility and Side Differences of Mechanical Tests for Determining the Structural Strength of the Proximal Femur», *J. Bone Miner. Res.*, vol. 19, n. 3, pagg. 379–385, dic. 2003, doi: 10.1359/JBMR.0301247.

[51] L. Grassi *et al.*, «Accuracy of finite element predictions in sideways load configurations for the proximal human femur», *J. Biomech.*, vol. 45, n. 2, pagg. 394–399, gen. 2012, doi: 10.1016/j.jbiomech.2011.10.019.

[52] M. M. Juszczyk, L. Cristofolini, e M. Viceconti, «The human proximal femur behaves linearly

elastic up to failure under physiological loading conditions», *J. Biomech.*, vol. 44, n. 12, pagg. 2259–2266, ago. 2011, doi: 10.1016/j.jbiomech.2011.05.038.

[53] J. Parkkari *et al.*, «Majority of Hip Fractures Occur as a Result of a Fall and Impact on the Greater Trochanter of the Femur: A Prospective Controlled Hip Fracture Study with 206 Consecutive Patients», *Calcif. Tissue Int.*, vol. 65, n. 3, pagg. 183–187, set. 1999, doi: 10.1007/s002239900679.

[54] H. L. Fermor *et al.*, «Biological, biochemical and biomechanical characterisation of articular cartilage from the porcine, bovine and ovine hip and knee», *Biomed. Mater. Eng.*, vol. 25, n. 4, pagg. 381–395, ago. 2015, doi: 10.3233/BME-151533.

[55] Z. Altai, M. Qasim, X. Li, e M. Viceconti, «The effect of boundary and loading conditions on patient classification using finite element predicted risk of fracture», *Clin. Biomech.*, vol. 68, pagg. 137–143, ago. 2019, doi: 10.1016/j.clinbiomech.2019.06.004.

[56] H. Gong, M. Zhang, Y. Fan, W. L. Kwok, e P. C. Leung, «Relationships Between Femoral Strength Evaluated by Nonlinear Finite Element Analysis and BMD, Material Distribution and Geometric Morphology», *Ann. Biomed. Eng.*, vol. 40, n. 7, pagg. 1575–1585, lug. 2012, doi: 10.1007/s10439-012-0514-7.

[57] H. H. Bayraktar, E. F. Morgan, G. L. Niebur, G. E. Morris, E. K. Wong, e T. M. Keaveny, «Comparison of the elastic and yield properties of human femoral trabecular and cortical bone tissue», *J. Biomech.*, vol. 37, n. 1, pagg. 27–35, gen. 2004, doi: 10.1016/S0021-9290(03)00257-4.

[58] M. N. Sarvi, Y. Luo, P. Sun, e J. Ouyang, «Experimental Validation of Subject-Specific Dynamics Model for Predicting Impact Force in Sideways Fall», *J. Biomed. Sci. Eng.*, vol. 07, n. 07, pagg. 405–418, 2014, doi: 10.4236/jbise.2014.77043.

[59] A. C. Laing e S. N. Robinovitch, «The Force Attenuation Provided by Hip Protectors Depends on Impact Velocity, Pelvic Size, and Soft Tissue Stiffness», *J. Biomech. Eng.*, vol. 130, n. 6, pag. 061005, dic. 2008, doi: 10.1115/1.2979867.

[60] S. N. Robinovitch, T. A. McMahon, e W. C. Hayes, «Force attenuation in trochanteric soft tissues during impact from a fall», *J. Orthop. Res.*, vol. 13, n. 6, pagg. 956–962, nov. 1995, doi: 10.1002/jor.1100130621.

[61] S. N. Robinovitch, W. C. Hayes, e T. A. McMahon, «Distribution of contact force during impact to the hip», *Ann. Biomed. Eng.*, vol. 25, n. 3, pagg. 499–508, mag. 1997, doi: 10.1007/BF02684190.

[62] A. J. van den Kroonenberg, W. C. Hayes, e T. A. McMahon, «Dynamic Models for Sideways Falls From Standing Height», *J. Biomech. Eng.*, vol. 117, n. 3, pagg. 309–318, ago. 1995, doi: 10.1115/1.2794186.